Geophys. J. Int. (2012) **189,** 967–983 doi: 10.1111/j.1365-246X.2011.05356.x

The effects of 3-D anelasticity (Q) structure on surface wave amplitudes

Youyi Ruan and Ying Zhou

Department of Geosciences, Virginia Polytechnic Institute and State University, Blacksburg, VA 24061*, USA. E-mail: chukren@vt.edu*

Accepted 2011 December 22. Received 2011 December 21; in original form 2011 March 21

SUMMARY

We investigate the effects of lateral perturbations in velocity and anelasticity (Q) on surface wave amplitudes based upon wave propagation simulations in 3-D earth models using a spectral element method (SEM). We construct 3-D Q models based upon a wave speed model S20RTS using a set of reasonable mineralogical parameters assuming lateral variations in both wave speed and anelasticity are due to temperature perturbations. We measure and compare amplitude perturbations of surface waves caused by 3-D wave speed (elastic) structures and those caused by 3-D anelastic (Q) structures at a period range of 50–200 s. The measurements show that influence of 3-D wave speed structures on amplitudes is comparable to that of 3-D Q structures at short period (50 s), but becomes dominant at longer periods. In ray theoretical framework, surface wave amplitudes can be decomposed into three terms—elastic focusing, anelastic attenuation and anelastic focusing—which depend, respectively, upon the roughness of phase velocity perturbations ($\partial_y^2 \delta \ln c$), perturbations in anelasticity ($\delta \ln Q^{-1}$) and the roughness of perturbations in anelasticity ($\partial_y^2 \delta \ln Q^{-1}$). Ray-theoretical calculations confirm the relative importance of 3-D Q and 3-D wave speed in perturbing surface wave amplitudes and show that anelastic focusing effects, which have been ignored in present-day tomographic studies, have a more significant effect than attenuation. Therefore, the effects of 3-D Q structures can be 'counter-intuitive' at long period for surface waves travelling through a low-Q region may experience amplitude increase.

Key words: Elasticity and anelasticity; Surface waves and free oscillations; Seismic attenuation; Seismic tomography.

1 INTRODUCTION

The anelasticity of Earth material causes energy dissipation of seismic waves through internal friction and it is often measured by the quality factor Q. In the past decades, progress made in mineral physics has allowed laboratory studies of anelasticity of upper-mantle minerals under high temperature and high pressure. Recent mineralogical experiments show that variations in temperature, water content and composition have very different effects on seismic wave speed and anelasticity in the Earth's mantle (e.g. Karato & Spetzler 1990; Isaak 1992; Jackson *et al.* 1992, 2002; Jackson 2000; Karato 2003; Faul & Jackson 2005). Therefore high-resolution 3-D anelastic structures, together with 3-D elastic wave speed structures, can provide important constraints on the thermal and chemical state of the Earth's interior.

The propagation of seismic waves can be affected by perturbations in both elastic and anelastic properties; therefore, seismic travel times and amplitudes depend upon both wave speed and anelasticity. In mapping lateral heterogeneities in the Earth's interior, seismic travel times are usually used to invert for wave speed and amplitudes are used to map anelasticity. In extending the finite-frequency theory of surface wave anelasticity (Dahlen & Zhou 2006) to account for anelastic dispersion, Zhou (2009) pointed out the importance of accounting for coupling of elastic and anelastic effects in both travel times and amplitudes and suggested that joint tomographic inversions of 3-D wave speed and 3-D anelasticity structures are necessary for long-period surface waves.

It has been long recognized that anelasticity can affect travel times of seismic waves through physical dispersion (e.g. Liu *et al.* 1976; Kanamori & Anderson 1977). However, in 3-D wave speed tomography, seismic travel times are typically used without considering anelastic dispersion caused by 3-D anelastic structures. Ruan & Zhou (2010) showed that physical dispersion due to lateral perturbations in Q can cause 15–20 per cent of observed phase delays (travel times) in long-period surface waves. Ignoring anelastic dispersion in surface wave inversions may therefore lead to biased tomographic models.

In resolving 3-D Q structures of the mantle, the difficulty is that elastic focusing and defocusing caused by 3-D wave speed structures can strongly affect seismic amplitudes (e.g. Woodhouse & Wong 1986; Romanowicz 1998; Selby & Woodhouse 2000; Dalton & Ekström 2006a,b; Yang & Forsyth 2006; Zhou 2009).

To date, the relative importance of elastic focusing and anelastic effects have not been well understood. In global anelastic tomography, different research groups take different approaches in handling elastic focusing/defocusing effects on amplitude (e.g. Durek *et al.* 1993; Romanowicz 1995; Bhattacharyya *et al.* 1996; Selby & Woodhouse 2002; Gung & Romanowicz 2004; Dalton & Ekström 2006b). The additional anelastic focusing/defocusing effects associated with anelastic dispersion have always been ignored. Although the resulting 3-D Q models are comparable in magnitude, large-scale features can differ greatly from each other (e.g. Gung & Romanowicz 2004; Dalton *et al.* 2008). More recently, there has been growing interest in modelling 3-D anelastic effects on seismic travel times and amplitudes through numerical wave propagation using currently available 3-D Q models (e.g. Savage *et al.* 2010).

In this study, we quantify the effects of anelastic (Q) and elastic structures on surface wave amplitudes through numerical wave propagation simulation using a spectral element method (Komatitsch & Tromp 1999, 2002a,b). Investigations of surface wave phase delays based upon the same simulations have been documented in Ruan & Zhou (2010). The effects of anelasticity are incorporated using an absorption band model with three standard linear solids (Savage *et al.* 2010). The Earth's bulk quality factor (Q_κ) is orders of magnitude larger than the shear quality factor (Q_μ), and the sensitivity of Rayleigh waves to perturbations in Q_κ is very weak; for Love waves, the sensitivity is zero. In this paper, we consider lateral heterogeneities only in Q_μ and ignore perturbations in Q_κ, and Q in this paper refers to Q_μ hereinafter. We simulate wave propagation in earth models with and without the presence of 3-D heterogeneities, and measure amplitude perturbations in fundamental-mode surface waves caused by 3-D wave speed structures as well as those caused by 3-D Q structures. Our amplitude measurements based on the 3-D models show that the effects of 3-D wave speed structures and 3-D Q structures are comparable in short-period surface waves, and the effects of 3-D wave speed structures are dominant in long-period surface waves.

In ray theory, amplitude perturbations due to 3-D heterogeneities can be decomposed into three contributing effects: elastic focusing and defocusing, anelastic attenuation and anelastic focusing and defocusing. We calculate ray theoretical amplitude perturbations in 3-D wave speed and 3-D Q models. Ray theoretical calculations confirm that elastic focusing dominates amplitude perturbations in 3-D models used in this study. In addition, we shows that the effects of anelastic attenuation are less significant compared to anelastic focusing/defocusing effects in long-period surface waves. Finally, we discuss the uncertainties in mineralogical parameters used in the numerical experiments.

2 WAVE PROPAGATION IN 3-D Q AND 3-D WAVE SPEED MODELS

In this section, we will briefly review earth models and numerical wave propagation experiments used to quantify the effects of 3-D anelasticity and 3-D wave speed structures on surface waves. The same models have been used to quantify the effects of anelastic dispersion on travel times in Ruan & Zhou (2010). We construct a 1-D reference Q model based upon a reference geotherm assuming half-space cooling of an adiabatic mantle. Parameters are shown in Table 1.

The reference geotherm profile is plotted in Fig. 1. The corresponding reference 1-D Q model then can be constructed from the reference geotherm assuming a thermally activated mechanism of anelasticity (Jackson & Anderson 1970; Karato & Spetzler 1990),

Table 1. Geothermal parameters used for reference temperature profile.

Parameters	Values
Surface temperature, T_s	0°C
Mantle temperature, T_m	1300°C
Thermal diffusivity, κ	1×10^{-6} m^2 s^{-1}
Cooling age, τ_c	60 Myr
Adiabatic gradient	0.5°C km^{-1}

$$Q(T) = A \exp\left[\frac{\alpha(E^* + PV^*)}{RT}\right], \tag{1}$$

where the activation energy $E^* = 470$ KJ mol^{-1} and activation volume $V^* = 17$ cm^3 mol^{-1} are estimated from laboratory studies of upper mantle minerals (e.g. olivine). The constant $A = 1.394$ is chosen so that the reference Q model is close to model PREM (Fig. 1).

Assuming a purely thermal origin of lateral perturbation in both wave speed and anelasticity (Q), we follow Ruan & Zhou (2010) and calculate temperature perturbations that correspond to shear wave speed perturbations in model S20RTS (Ritsema & Van Heijst 2000) using the temperature partial derivative of shear wave speed (e.g. Karato 1993; Ruan & Zhou 2010),

$$\frac{\partial \ln V}{\partial T} = \frac{\partial \ln V_0}{\partial T} - \frac{1}{Q\pi}\frac{E^* + PV^*}{RT^2}. \tag{2}$$

The temperature partial derivative $\partial \ln V/\partial T$ depends on Q, and an iterative approach was used to compute perturbations in Q. The rms of the wave speed and Q models are plotted in Fig 1 as a function of depth, and 3-D wave speed and 3-D Q maps at a depth of 100 km are plotted in Figs 2(a) and (b). The rms strength of $\delta \ln Q^{-1}$ in the Q model is comparable to recent tomographic 3-D Q models (e.g. Dalton *et al.* 2008). Assuming current global tomographic 3-D Q models are correct in order of magnitude, our 3-D Q model should be reasonable for the investigation of 3-D anelastic effects on surface waves. The advantage of using the wave speed-converted Q model is that the Q model is highly correlated with the 3-D wave speed model S20RTS, which allows us to investigate correlations between their corresponding effects.

We investigate the effects of 3-D wave speed and 3-D Q structures on surface wave amplitudes through wave propagation simulation in four different earth models (Table 2) using a spectral element method (Komatitsch & Tromp 1999, 2002a,b). To examine the elastic focusing/defocusing effects on surface wave amplitudes due to 3-D wave speed structures, we measure amplitude differences between synthetic seismograms generated in model (I)—1-D velocity and 1-D Q (PREM) and model (II)—3-D velocity and 1-D Q (S20RTS). The Q structures in model (I) and (II) are identical; therefore, the measured perturbations in surface wave amplitudes are due to the 3-D velocity structures, that is, $(A_{3-\mathrm{DV}} - A_{1-\mathrm{DV}})/A_{1-\mathrm{DV}}$ or *elastic* $\delta \ln A$. In the case of examining the effects of 3-D Q structures ('anelastic effects' hereinafter), we measure amplitude perturbations between synthetic seismograms generated in model (III)—3-D velocity and 1-D Q and model (IV)—3-D velocity and 3-D Q. The velocity structures are identical in these two models so amplitude perturbations are due to 3-D Q structures, that is, $(A_{3-\mathrm{DQ}} - A_{1-\mathrm{DQ}})/A_{1-\mathrm{DQ}}$ or *anelastic* $\delta \ln A$. The 1-D and 3-D Q models are shown in Figs 1 and 2.

We use 12 earthquake events and 801 seismic stations in numerical simulations to provide a good global path coverage (Fig. 2). For

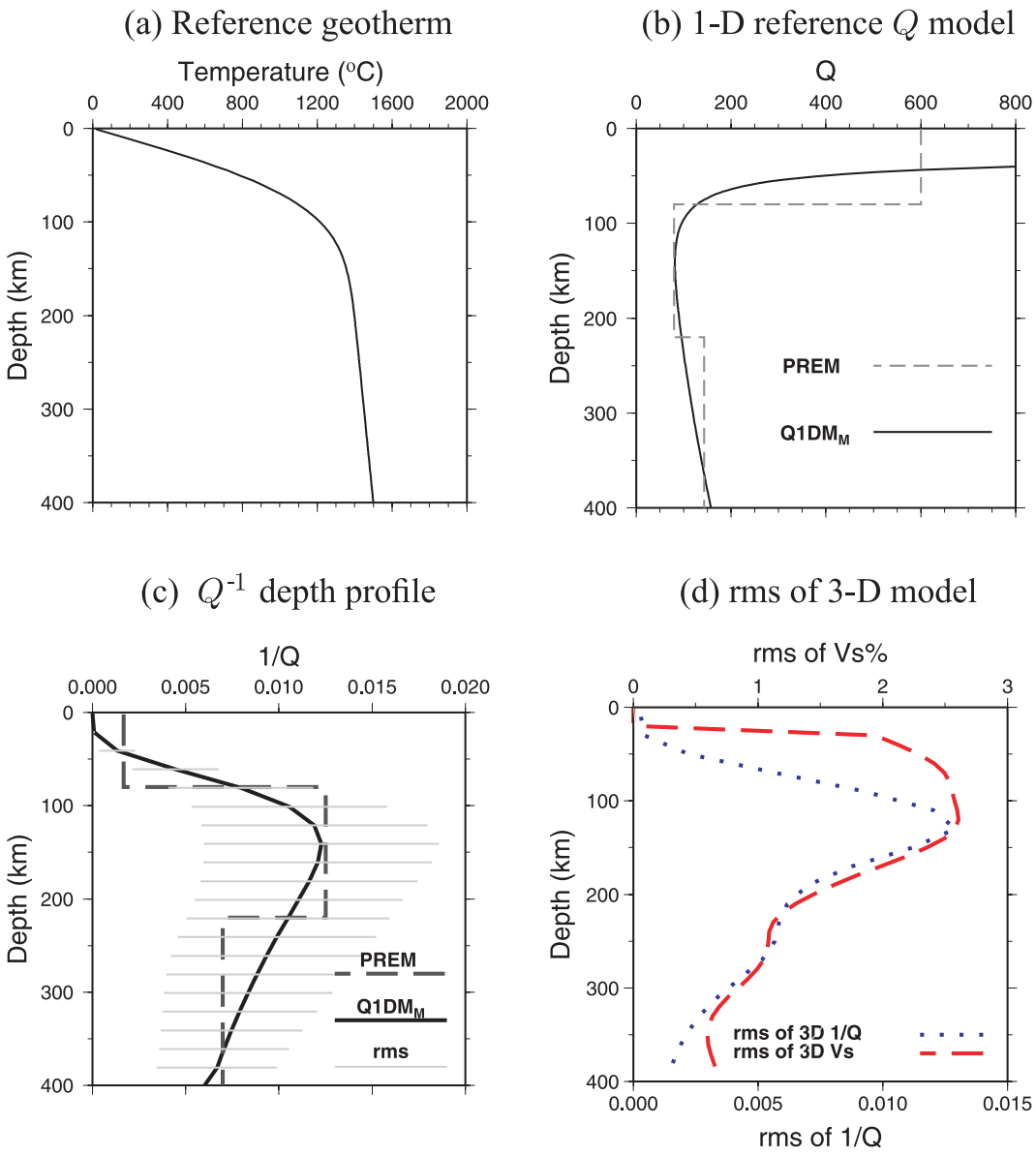

Figure 1. (a) Reference 1-D temperature model derived assuming half-space cooling of an adiabatic mantle. Adiabatic thermal gradient is 0.5°C km^{-1}, and geothermal parameters are shown in Table 1. (b) Reference Q model (Q_μ) constructed using the reference geotherm and mineralogical parameters $E^* = 470$ KJ mol^{-1} and $V^* = 17$ cm^3 mol^{-1}. PREM Q_μ is also shown in dashed line for reference (Dziewonski & Anderson 1981). (c) Depth profile of $1/Q$ where grey bars indicate rms variations of $1/Q$ at various depths in 3-D Q model. (d) rms of 3-D wave speed and Q models as a function of depth.

each event, wave propagation simulations are run for all four models in Table 2. Examples of synthetic seismograms from SEM simulations and associated ray paths are plotted in Fig. 3. The transverse and vertical component seismograms at station BMN have been bandpass filtered between 8 and 15 mHz. The top two seismograms in Figs 3(a) and (b) show amplitude perturbations caused by 3-D Q structures, while the bottom two seismograms show amplitude perturbations caused by 3-D wave speed structures. Amplitude variations measured at a period of 100 s (10 mHz) are shown beneath each two traces. For the transverse component (Love waves), lateral variations in Q cause a 3.5 per cent increase in amplitude while variation in wave speed cause a 133.7 per cent increase in amplitude. In the vertical component Rayleigh waves, the 3-D Q and 3-D wave speed structures increase amplitude by -1.3 and 42.5 per cent, respectively. This indicates elastic effects on surface wave amplitudes, that is, focusing/defocusing, can be much stronger than anelastic attenuation. In this example, both Love waves and Rayleigh waves show a strong elastic focusing (amplification) on amplitudes as they propagate through strong slow anomalies. We assume lateral heterogeneities in the earth models are thermally originated, therefore a slow anomaly is associated with a low Q anomaly where strong anelastic attenuation is expected (decrease in amplitude). However, synthetic seismograms show a slight increase in the amplitude of Love waves and a negligible decrease in the amplitude of Rayleigh waves. Such unexpected variation indicates anelastic focusing effects associated with physical dispersion are strong enough to cancel out the attenuation effects. The details of wave focusing effects associated with anelastic dispersion will be discussed in Section 5. Amplitude measurements as a function of wave period are shown in Figs 3(d) and (e) for Love waves and Rayleigh waves, respectively.

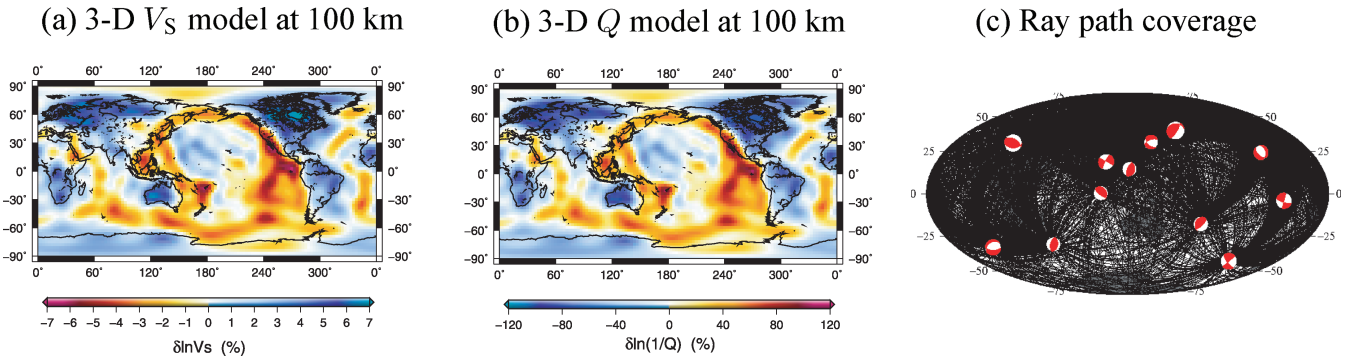

Figure 2. (a) 3-D shear wave speed model S20RTS (Ritsema & Van Heijst 2000) at a depth of 100 km. (b) 3-D anelasticity (Q) model at a depth of 100 km, the perturbation magnitude of Q^{-1} are comparable to recent tomographic models (e.g. Dalton *et al.* 2008). Note that perturbations in Q model and wave speed model are correlated as we assume both of them are caused by temperature variations. (c) Ray paths used in numerical simulations. Locations and focal mechanisms of the twelve earthquakes are indicated by beach balls.

The strong frequency dependence of amplitude perturbations will be discussed in Sections 4 and 5.

3 MEASUREMENTS OF SURFACE WAVE AMPLITUDE VARIATIONS

To reduce bias in spectral estimation, we measure surface wave amplitude perturbations using a multitaper method (MTM) (Laske & Masters 1996; Zhou *et al.* 2004). In this study, five 2.5-π prolate spheroidal eigentapers (Slepian 1978) are used. Seismograms measured with these eigentapers have their spectra narrowly concentrated around the central frequency. Amplitude perturbations and associated errors are estimated by least-square fitting of measurements made with the five orthogonal tapers. We measure fundamental-mode surface wave amplitude perturbations at frequencies (periods) from 5 mHz (200 s) to 20 mHz (50 s).

Time windows are chosen for each seismogram to include group arrivals of surface waves at the periods of measurement, and to exclude higher-mode surface waves whenever possible. The spectra of windowed seismograms depend on the time window applied in making measurements. To examine the effects of windowing on amplitude measurements, we compare amplitude perturbations of 100 s Rayleigh waves measured with different time windows. We start with a measurement window that is approximately five times as long as the period of the wave (∼500 s) centred at the arrival of the fundamental-mode surface wave, we then extend the length of the window by 150 s in both directions to make it a longer window (∼800 s) and the third measurement window is 1100 s centred at the same arrivals. Examples of measurement time windows as well as amplitude variations caused by measurement time windows are shown in Fig. 4. Overall, amplitude variations due to differences in window length can be significant, especially when windows are extended to include higher-mode energy. A longer time window can increase the resolution of amplitude spectra, however, it may also increase the risk of higher-mode contamination. In this study, we carefully choose measurement windows to strike a balance between good spectra resolution and minimum higher-mode contamination. Due to the dispersion of surface waves, we select measurement windows based on visual examination of seismograms band-pass filtered at two different frequency bands, 20–10 mHz (50–100 s) and 5–10 mHz (100–200 s). The final hand-picked measurement windows range from 600 to 800 s in the period range between 50 and 100 s and the window length varies from 1000 s to 1600 s in the period range between 100 and 200 s, respectively.

Table 2. Models used for 3-D SEM wave propagation simulation.

	Model	Velocity	Anelasticity (Q)
Elastic effects	I	1-D (PREM)	1-D (PREM)
	II	3-D (S20RTS)	1-D (PREM)
Anelastic effects	III	3-D (S20RTS)	1-D ($Q1DM_M$)
	IV	3-D (S20RTS)	3-D ($Q3DM_M$)

Fundamental-mode surface waves in model PREM and S20RTS have different group arrival times. This often makes it difficult to exclude higher-mode surface waves in determining the time window for measurements, especially in the case of Love waves. To examine the possible effects of including higher-mode surface waves in the measurement window, we compare measurements made with and without higher-mode surface waves. In the case with higher modes, we measure amplitude perturbations between seismograms generated in model PREM and S20RTS using SEM; therefore, both seismograms include all seismic phases. In the case without higher modes, we measure amplitude perturbations between fundamental-mode-only seismograms generated in model PREM based on surface wave mode calculations and seismograms generated in model S20RTS using SEM. Amplitude measurements made with and without higher modes for 100 s Love waves and Rayleigh waves are shown in Fig. 5. Higher-mode surface waves have some effects on Rayleigh wave amplitudes (Fig. 5b), but in general they are not significant compared to uncertainties in measurements. The effects of higher-mode surface waves are stronger in Love waves than in Rayleigh waves (Fig. 5a). This is expected because fundamental-mode Rayleigh waves travel much slower than higher-mode Rayleigh waves, but the difference in travelling speed between fundamental-mode and higher-mode Love waves are much smaller and therefore they are not well separated in seismograms. It is also noteworthy that amplitudes of fundamental-mode and higher-mode surface waves are caused by the same subsurface structures but they have different depth sensitivity. Unless the structure varies rapidly with depth, bias introduced by high-mode contamination will be limited, as shown in Fig. 5. In Fig. 5, the calculations are for an extreme case and effect of higher-mode contamination is, in general, less significant in the measurements that we will discuss in Section 4.

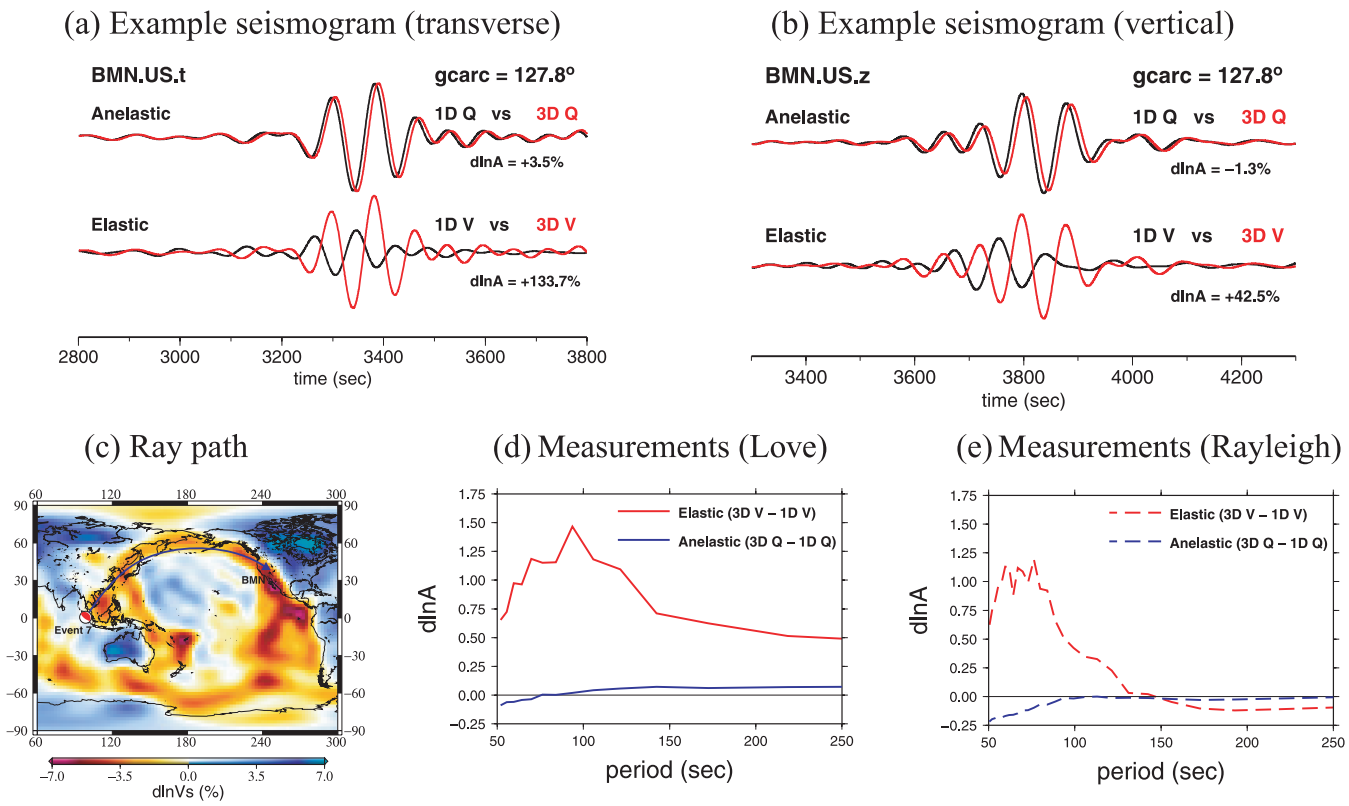

Figure 3. (a) Transverse and (b) vertical components of synthetic seismograms at station BMN, bandpass filtered between 8 and 15 mHz. Top seismogram pairs show effects due to anelastic perturbations, black seismograms are generated using model (III): 3-D velocity and 1-D Q, red seismograms are generated using model (IV): 3-D velocity and 3-D Q. Bottom seismogram pairs show differences due to elastic perturbations: black seismograms are generated using model (I): 1-D velocity and 1-D Q; red seismograms are generated using model (II): 3-D velocity and 1-D Q. Amplitude perturbations measured at 100 s using a multitaper technique are indicated below the trace pairs. The ray path of the seismograms is shown in (c) and measured elastic and anelastic amplitude perturbations as a function of period are plotted in (d) for Love waves and (e) for Rayleigh waves.

The excitation of surface wave amplitudes by a moment tensor source depends on local structure at the source. In 3-D models, local structures in source regions are often different from that in 1-D models. In Fig. 6, we show that the effects of source radiation differences on surface wave amplitudes are not significant as we have excluded paths close to nodal planes where source local structures may have stronger influences on source excitations. The amplitude variations due to direct source excitation differences are generally smaller than measurement error bars.

4 3-D ANELASTIC EFFECTS ON SURFACE WAVES AND FREQUENCY DEPENDENCE

It is well known that amplitudes of seismic waves can be affected by the magnitude of earthquakes, geometrical spreading, source radiation pattern, wave attenuation and focusing/defocusing effects. In this study, we focus on amplitude perturbations caused by wave attenuation and focusing/defocusing effects, and quantify the effects of 3-D wave speed and 3-D Q structure as a function of wave period. Lateral perturbations in wave speed affect the amplitude of seismic waves through elastic focusing/defocusing without energy loss. In the presence of 3-D anelastic heterogeneities, amplitude of seismic waves can be attenuated due to energy loss caused by internal friction in mantle materials. In addition to anelastic attenuation, anelastic structures also cause physical dispersion, introducing additional focusing/defocusing effects which we have referred to as 'anelastic focusing/defocusing'. Anelastic focusing/defocusing effects strongly depend upon wave frequency because of physical dispersion. It is worth emphasizing that this type of focusing effects is associated with 3-D Q structures.

In Fig. 7, we compare Love- and Rayleigh-wave amplitude variations caused by 3-D wave speed structures, elastic $\delta \ln A$ and those caused by 3-D Q structures, anelastic $\delta \ln A$. Vertical and horizontal coordinates in the scatterplot represent elastic $\delta \ln A$ and anelastic $\delta \ln A$ measured for the same source–receiver pair. Black crosses on each dot show measurement errors estimated using multitaper technique. We have excluded measurements with large error bars, which leaves approximately 3000–6000 measurements in each scatterplot.

Our measurements show that 3-D anelastic effects on surface wave amplitudes are frequency-dependent; anelastic effects in long-period surface waves are much weaker than those in short-period surface waves. For 50-s Love waves, anelastic effects on amplitude are comparable to elastic effects, and they are, in general, negatively correlated. For surface waves at longer periods (100 and 200 s), 3-D Q structures cause much smaller amplitude perturbations than 3-D wave speed structures, that is, anelastic effects on amplitudes are much weaker than elastic focusing. In addition, the correlation between anelastic effects and elastic focusing is positive, indicating that the dominant effect of 3-D Q structures is anelastic focusing rather than attenuation as anelastic focusing correlates positively with elastic focusing. Similar patterns are seen in Rayleigh waves.

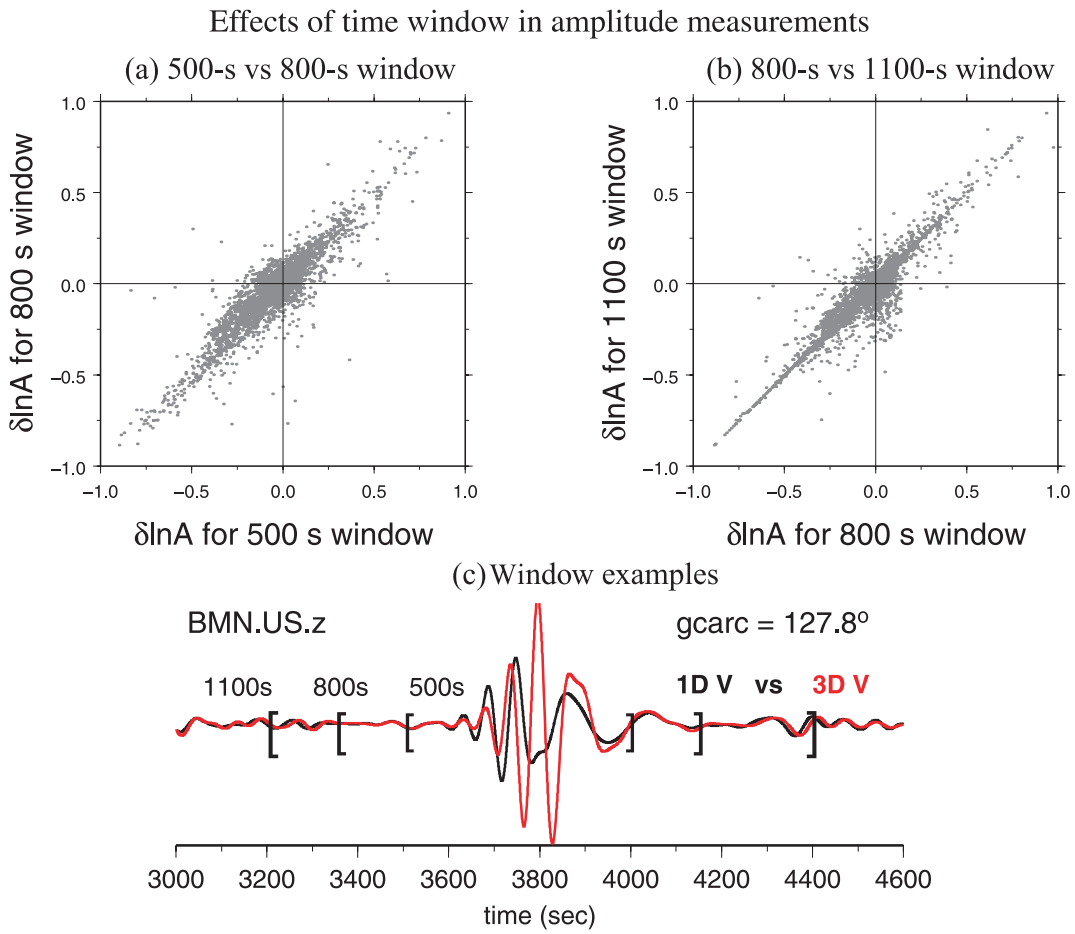

Figure 4. Comparison of elastic amplitude variations ($(A_{3DV} - A_{1DV})/A_{1DV}$) of 100 s Rayleigh waves measured with different time windows. (a) Shows amplitude perturbations measured using 500 s time windows plotted against measurements made with 800 s time windows, and (b) is the same as (a) but for 800 s time windows and 1100 s time windows. Examples of time windows are shown in (c) for a seismogram at station BMN. The seismogram is the same as in Fig. 3(b) but bandpass filtered between 4 and 20 mHz. Amplitude perturbations measured using different windows show significant differences, especially when the time window is long enough to include significant higher-mode energy. Time windows in our study are chosen to provide a good spectra resolution but minimum higher-mode contamination.

In 50-s Rayleigh waves, the effects of 3-D wave speed and 3-D Q structures are about equally important, and they show roughly a negative correlation. In 100- and 200-s Rayleigh waves, anelastic effects become much weaker than elastic focusing/defocusing effects, and correlate positively with elastic focusing effects.

To better illustrate the relative importance of elastic and anelastic effects, we calculate the average absolute amplitude perturbations caused by 3-D wave speed and 3-D Q structures at periods of 50, 100, 150 and 200 s (Fig. 8). The average absolute amplitude perturbation is defined as

$$|\delta \ln A|_{\text{ave}} = \frac{1}{N}\sum_{i=1}^{N} |\delta \ln A_i|. \tag{3}$$

The black bars in Fig. 8 indicate amplitude perturbations caused by 3-D wave speed structures (elastic $\delta \ln A$), while the grey bars are those caused by 3-D Q structures (anelastic $\delta \ln A$). At all periods, elastic $\delta \ln A$ is larger than anelastic $\delta \ln A$ except for short-period (50 s) Rayleigh waves where anelastic effects on amplitudes are comparable to elastic focusing effects. This is expected because 50 s Rayleigh waves are most sensitive to the low Q zone (Fig. 7), and therefore experience strongest attenuation in amplitude. At longer periods (>100 s), anelastic effects decrease very quickly with increasing wave period, and elastic focusing/defocusing effects dominate surface wave amplitude variations. We conclude that focusing/defocusing caused by 3-D wave speed structures are the dominant effects in surface wave amplitudes, tomographic studies without full consideration of focusing/defocusing effects may strongly bias tomographic results. In current 3-D Q tomographic studies, elastic focusing/defocusing effects are sometimes ignored (e.g. Gung & Romanowicz 2004). This does not simply imply that tomographic Q perturbations have been overestimated because tomography is often an ill-posed problem due to limited data coverage, noise in data as well as errors in tomographic theory. How errors in tomographic theory are mapped into tomographic models depends on regularization (damping or smoothing) applied in inversions.

The correlation between elastic and anelastic effects on amplitude variations is frequency-dependent (Fig. 7). At 50 s, the correlation between anelastic and elastic effects is largely negative, while at longer periods (>100 s) the correlation becomes positive. We have assumed lateral heterogeneities in the models are purely thermal; therefore, a slow anomaly is associated with a hot region where strong attenuation is expected. A slow anomaly along a ray path will result in elastic focusing (amplification) and therefore an

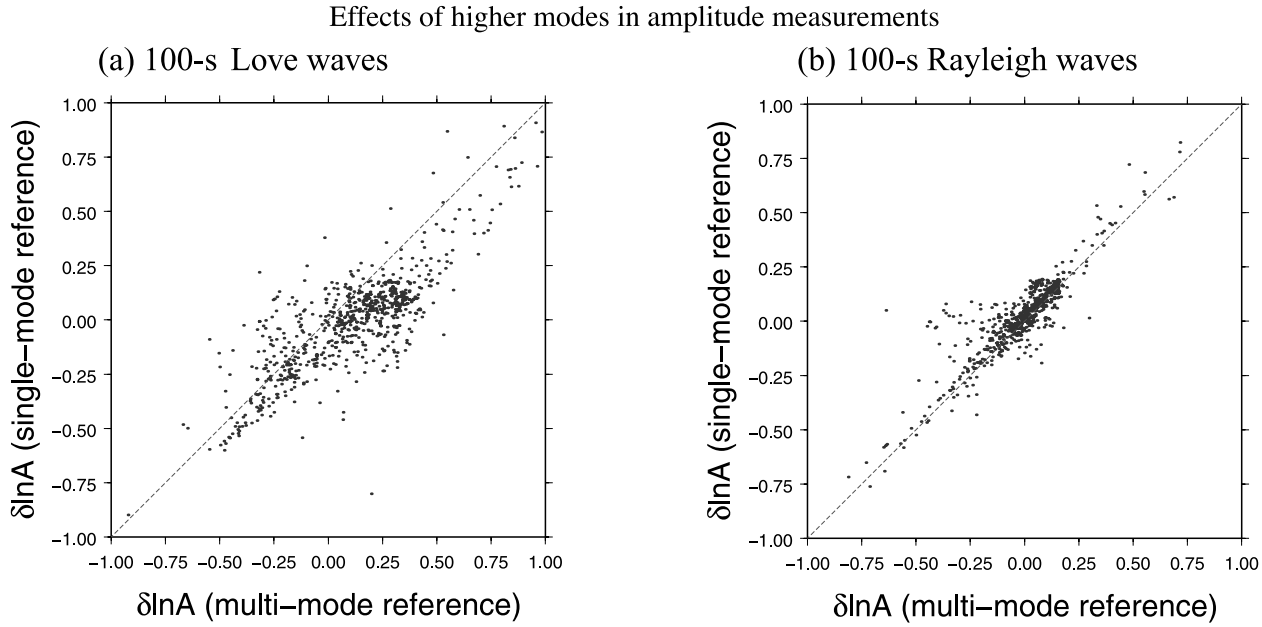

Figure 5. Comparison between amplitude perturbation measurements with and without higher-mode surface wave effects. (a) Amplitude measurements made using single-mode reference seismograms plotted against measurements made with multimode reference seismograms for 100-s Love waves. In single-mode reference measurements, $\delta \ln A$ is measured between fundamental-mode-only seismograms generated in PREM using surface wave mode calculations and seismograms generated in model S20RTS using SEM. In multimode reference measurements, $\delta \ln A$ is measured between seismograms generated in PREM and S20RTS using SEM. Panel (b) is the same as (a) but for 100-s Rayleigh waves.

increase in amplitude, while the higher-than-normal temperature of the anomaly will lead to stronger anelasticity. If we assume the dominant effect of a low Q region is anelastic attenuation, an *increase* in elastic $\delta \ln A$ should correspond to a *decrease* in anelastic $\delta \ln A$, and one should expect a 'negative' correlation between anelastic and elastic effects on amplitude.

At short period (50 s), the correlation between elastic focusing and anelastic effects is in general negative, the correlation coefficient is -0.05 in Love waves and -0.38 in Rayleigh waves. It is known that elastic focusing/defocusing effects are associated with the roughness (second spatial derivative) of 3-D wave speed structures and the attenuation of amplitudes is associated with 3-D Q structures; lateral variations in Q structures and roughness of wave speed structures are not necessarily well correlated, which explains the small correlation coefficients at short periods where anelastic effects are dominated by wave attenuation.

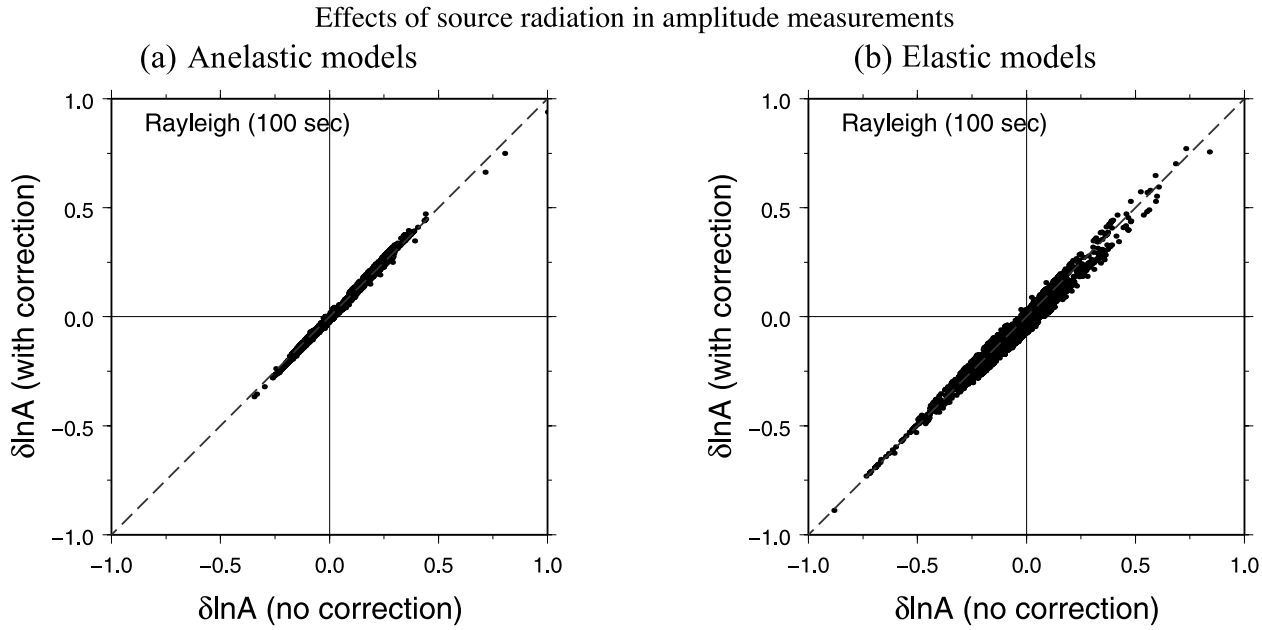

Figure 6. Examples of 100-s Rayleigh-wave amplitude measurements made with and without corrections of source radiation differences between 1-D and 3-D models for (a) anelastic models and (b) elastic models. The effects of source radiation differences on amplitudes are not significant compared to measurement error bars.

The correlation between anelastic and elastic effects becomes positive in long-period surface waves (100 and 200 s). While the positive correlation seems to be 'counter-intuitive', it can be well explained by 3-D anelastic focusing/defocusing effects associated with additional wave speed perturbations caused by physical dispersion. In anelastic material, relaxation of elastic moduli depends upon the frequency of the waves, resulting in frequency-dependent wave speed, that is, anelastic dispersion (Dahlen & Tromp 1998)

$$c(\omega) = c(\omega_0)\left[1 + \frac{1}{\pi Q}\ln\left(\frac{\omega}{\omega_0}\right)\right], \quad (4)$$

where $c(\omega_0)$ is the wave speed at a reference angular frequency ω_0, and Q is the quality factor. In the presence of 3-D Q anomalies, anelastic focusing effects are associated with the roughness (second spatial derivative) of 3-D Q structures. In our earth model, lateral perturbations in Q and wave speed structures are well correlated, so do the roughness structures of 3-D Q and 3-D wave speed models, therefore a positive correlation between elastic focusing and anelastic effects is expected when the dominant effect of 3-D Q structures is anelastic focusing. At long period (>100 s), the positive correlation indicates 3-D Q structures affect surface wave

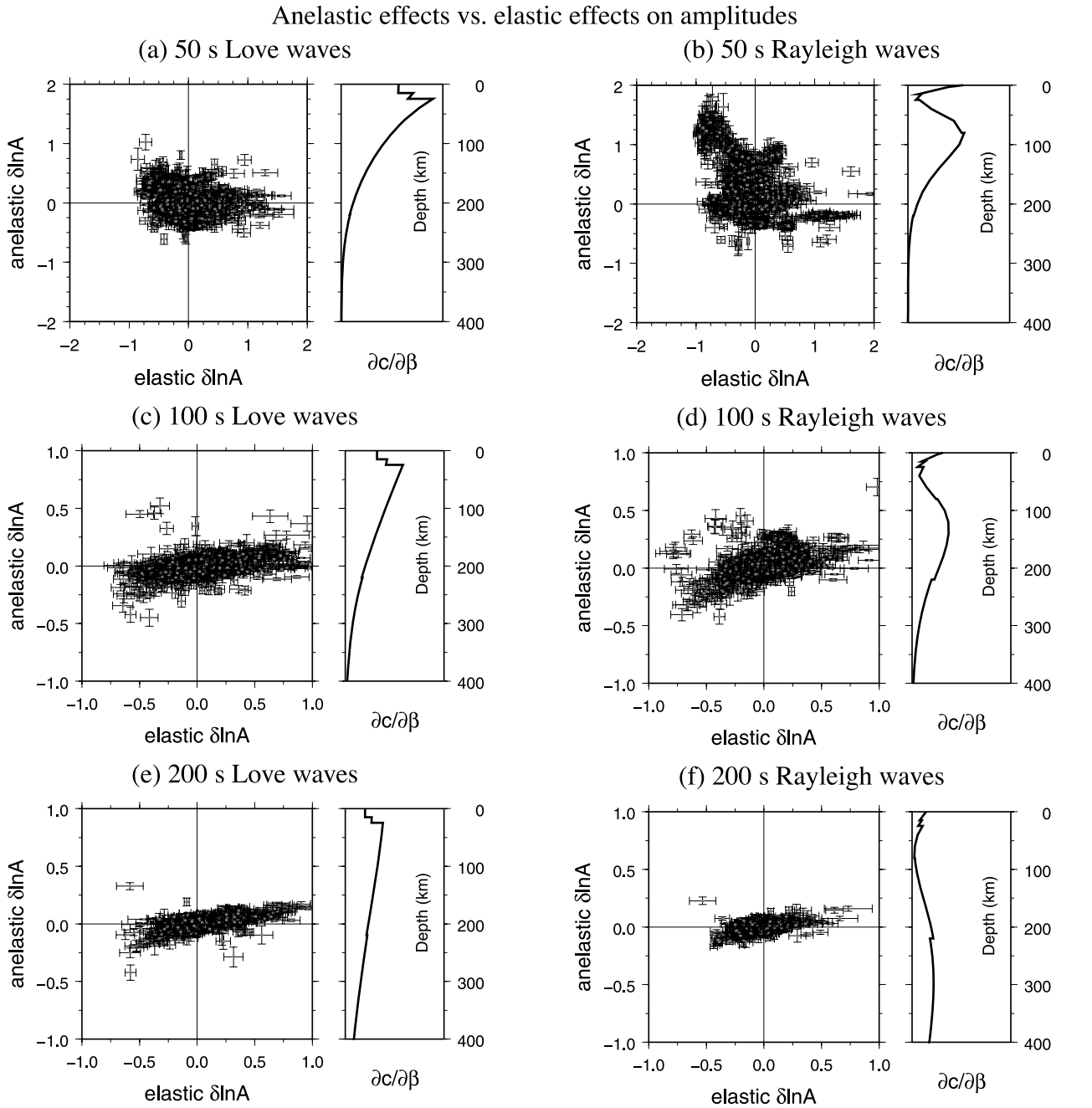

Figure 7. Comparison between anelastic and elastic effects on Love- and Rayleigh-wave amplitudes at periods of 50, 100 and 200 s. Measurement error bars are estimated from multitaper analysis. Radial sensitivity ($\partial c/\partial \beta$) of fundamental-mode Love and Rayleigh waves are also plotted for reference. At 50 s, the anelastic effects on amplitudes are comparable to elastic effects, they are in general negatively correlated. At longer periods (100 and 200 s), anelastic effects become weaker with increasing wave period, and begin to show a positive correlation with elastic effects. Anelastic effects in 50 and 100 s Rayleigh waves are stronger than in Love waves due to its stronger sensitivity to the low Q zone.

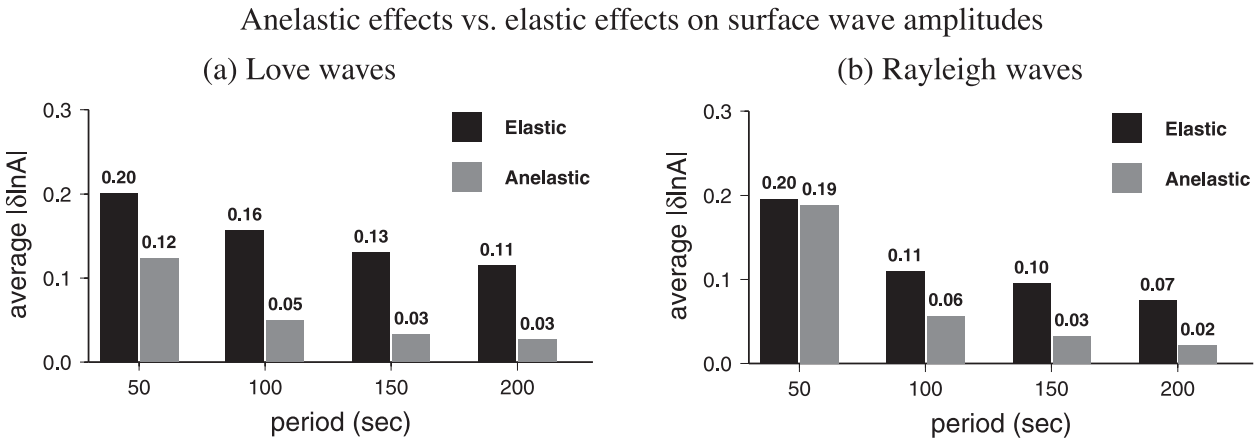

Figure 8. Comparison between the anelastic and elastic effects on surface wave amplitudes as a function of periods. The average amplitude perturbations, $|\delta \ln A|$, are calculated using eq. (3). Anelastic effects are less significant than elastic focusing on amplitudes except for in short-period (50 s) Rayleigh waves.

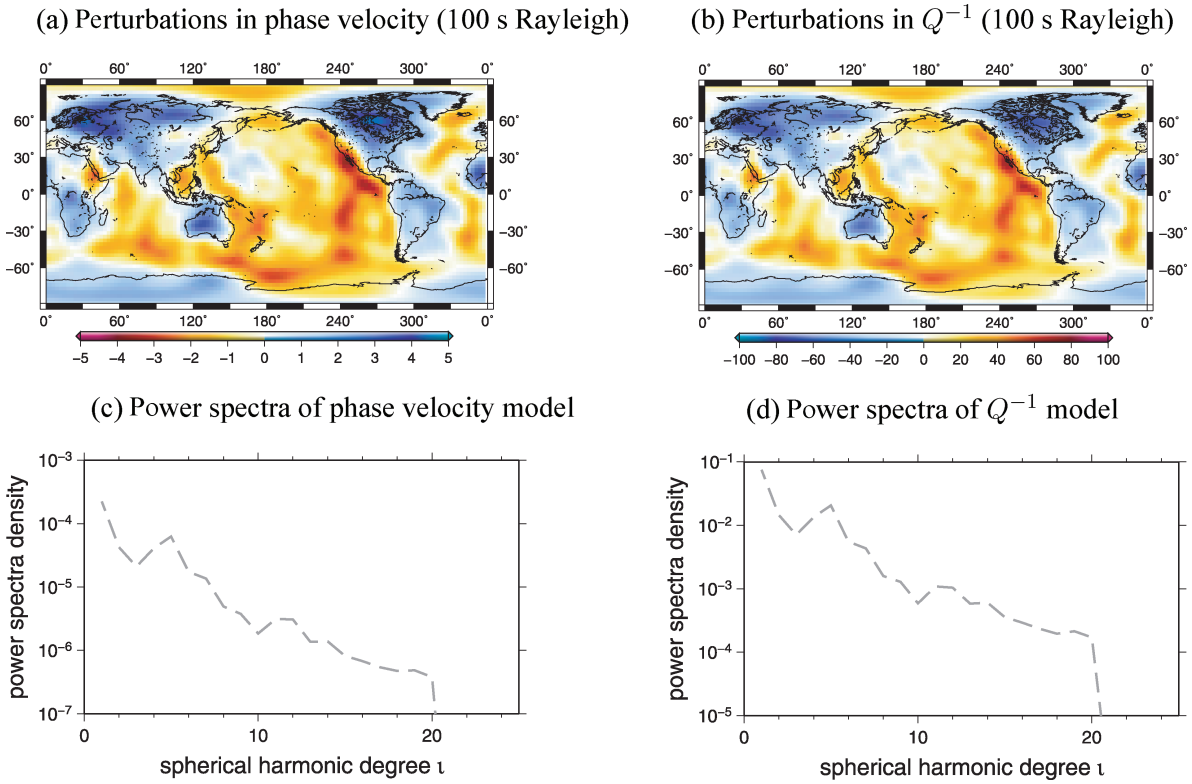

Figure 9. (a) Perturbations in 100 s Rayleigh-wave phase velocity due to 3-D wave speed structures. (b) Perturbations in 100 s Rayleigh-wave Q^{-1} due to 3-D Q structures; (c) and (d) are the corresponding power spectra [eq. (9)] of perturbations in phase velocity and Q^{-1}. Power density of perturbations in both phase velocity and Q^{-1} models decreases with increasing harmonic degree, indicating that long-wavelength anomalies are dominant in both models.

amplitudes mainly through anelastic focusing and anelastic attenuation is minimum.

It is worth noting that wave speeds in anelastic media have been decomposed into 'elastic speed' (speed at a reference frequency) and 'anelastic speed' associated with additional physical dispersion. At the reference frequency ω_0, 'anelastic speed' is strictly zero and independent of Q perturbations (eq. 4). The effects of Q perturbations on wave speed at the reference frequency are included in 'elastic wave speed'. If the reference frequency is close to the high-frequency end of a mantle absorption band model, the 'elastic speed' will be close to wave speed associated with unrelaxed modulus. In this paper, we have chosen a reference frequency of 1 Hz for two reasons: (1) mantle models are often developed at a reference frequency of 1 Hz due to limited bandwidth of teleseismic data and (2) our calculations at 1-Hz reference frequency will provide a lower limit estimates of 3-D anelastic dispersion effects in surface wave amplitudes.

5 RAY THEORETICAL PREDICTIONS OF SURFACE WAVE AMPLITUDES

In a 3-D earth model with lateral variations in both wave speed and anelasticity (Q), amplitude perturbations can be decomposed into

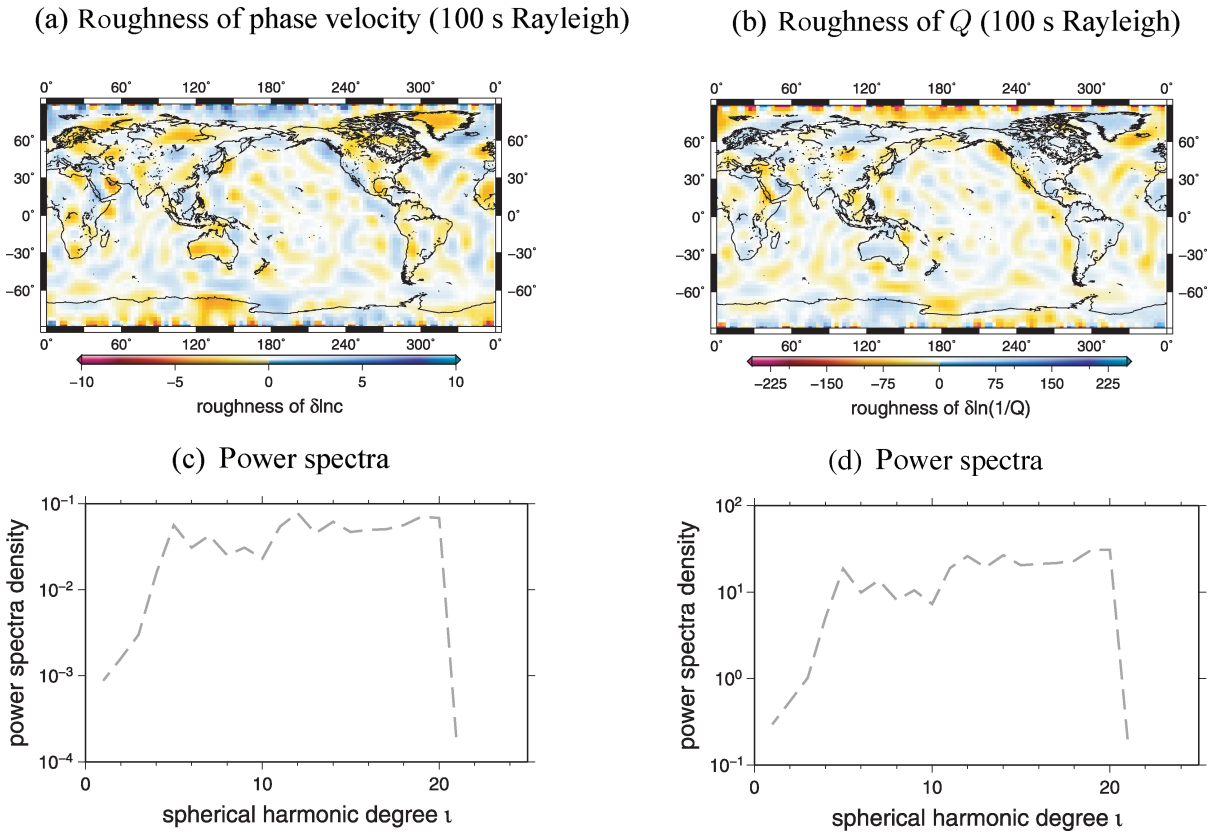

Figure 10. Roughness of perturbations in (a) phase velocity and (b) Q^{-1} models for 100-s Rayleigh waves. Panels (c) and (d) are their corresponding power spectra, both show a flat spectra between harmonic degree 5 and 20, indicating larger-scale structures ($l < 5$) are relatively insignificant in the roughness maps. Two roughness maps are well correlated with a correlation coefficient of −0.99.

three components in the framework of ray theory (Zhou 2009),

$$\delta \ln A = \delta \ln A_{V\text{foc}} + \delta \ln A_{Q\text{att}} + \delta \ln A_{Q\text{foc}}. \tag{5}$$

The first term,

$$\delta \ln A_{V\text{foc}} = \frac{1}{2 \sin \Delta} \int_0^{\Delta} \sin x \, \sin(\Delta - x) \partial_y^2 \frac{\delta c}{c} \, \mathrm{d}x, \tag{6}$$

is the elastic focusing/defocusing term which depends on the roughness (second spatial derivatives) of perturbations in phase velocity ($\delta c/c$).

The second term,

$$\delta \ln A_{Q\text{att}} = -\frac{\omega}{2CQ} \int_0^{\Delta} \frac{\delta Q^{-1}}{Q^{-1}} \, \mathrm{d}x, \tag{7}$$

accounts for wave attenuation which depends upon the perturbations of anelasticity (δQ^{-1}).

The third term,

$$\delta \ln A_{Q\text{foc}} = \frac{c}{2\pi C Q \sin \Delta} \ln\left(\frac{\omega}{\omega_0}\right) \int_0^{\Delta} \sin x \, \sin(\Delta - x) \partial_y^2 \frac{\delta Q^{-1}}{Q^{-1}} \, \mathrm{d}x, \tag{8}$$

accounts for anelastic focusing/defocusing and depends upon the roughness of perturbations in anelasticity. In the above equations, Δ is epicentral distance in radian, c and C are local phase and group velocities measured in radians per second on the unit sphere, Q is local Love-wave or Rayleigh-wave quality factor, ω is angular frequency and integrations are along the great circle ray path. It is worth emphasizing again that anelastic focusing in this paper is defined with respect to the reference frequency ω_0. At the reference frequency, the third term is zero, it does not indicate that Q perturbations have no affect on amplitudes through anelastic focusing but that the effects have been included in 'elastic focusing' caused by perturbations in 'elastic speed' (speed at the reference frequency).

To calculate the ray theoretical surface wave amplitude variations caused by 3-D wave speed and 3-D Q structures, we construct local 1-D wave speed and Q models on $2^\circ \times 2^\circ$ cells. This produces 16 200 1-D local models for each of the 3-D models shown in Table 2. For each 1-D model, we calculate phase velocities and Q values for both Love waves and Rayleigh waves at periods of 50, 100, 150 and 200 s by solving radial equations for spherically symmetrical earth models. Phase velocity maps ($\delta c/c$) associated with 3-D wave speed structures are calculated based on model I and model II (Table 2).

Example phase velocity maps ($\delta c/c$) and Q maps ($\delta Q^{-1}/Q^{-1}$) are shown in Figs 9(a) and (b) for 100 s Rayleigh waves. They are well correlated because both are derived from a thermal model. Note that fractional perturbations in Q^{-1} are about one order of magnitude stronger than those in phase velocity. The power spectra of the phase velocity and Q maps are calculated as

$$P_l = \frac{1}{2l+1}\left[a_{l0}^2 + \sum_{m=1}^{l}(a_{lm}^2 + b_{lm}^2)\right], \tag{9}$$

where a_{lm} and b_{lm} are the coefficients when the maps are decomposed using the real spherical harmonics (Dahlen & Tromp 1998, Appendix B),

$$\psi(\theta, \phi) = \sum_{l=0}^{\infty}\left[a_{l0}X_{l0} + \sqrt{2}\sum_{m=1}^{l} X_{lm}(a_{lm}\cos m\phi + b_{lm}\sin m\phi)\right], \tag{10}$$

where $\psi(\theta, \phi)$ represents the perturbation field of phase velocity or Q^{-1}. The power spectra are plotted in Figs 9(c) and (d) for 100 s Rayleigh waves. The power spectra of perturbations in both phase velocity and Q^{-1} show that long-wavelength anomalies ($l <$ 10) are dominant features in both models and the power spectra in general decrease with harmonic degree. Roughness of perturbations in phase velocity and Q^{-1} (second spatial derivative) are calculated using surface Laplacian

$$\nabla^2\psi = \frac{\partial^2\psi}{\partial\theta^2} + \cot\theta\frac{\partial\psi}{\partial\theta} + \frac{1}{\sin^2\theta}\frac{\partial^2\psi}{\partial\phi^2}.$$

Example roughness maps for 100 s Rayleigh waves are shown in Fig. 10. For both Q^{-1} and phase velocity models, the roughness maps show much smaller-scale structure, and unlike the perturbation maps (Fig. 9) there is no apparent difference between oceans and continents. The roughness map of Q^{-1} and the roughness map of phase velocity are well correlated, and both roughness maps have flat spectra between degree 5 and 20; the largest scale structures ($l <$ 5) are relatively insignificant in roughness maps. Given that model S20RTS contains structures limited to harmonic degree $l \leq 20$, we do not expect smaller-scale structures in both phase velocity and Q^{-1} models and their roughness maps.

To calculate ray theoretical predictions, we compute the second spatial partial derivative (roughness) of $\delta c/c$ and $\delta Q^{-1}/Q^{-1}$ in the direction perpendicular to the geometrical ray path in the ray coordinates by rotating the coordinates such that the source and receiver are on the equator (see Appendix). Ray theoretical calculations of amplitude perturbations confirm: (1) elastic focusing/defocusing effects caused by 3-D wave speed structures dominate amplitude variations; and (2) anelastic effects caused by 3-D Q structures are important at 50 s but decrease quickly at longer periods. Fig. 11 shows the predicted 3-D elastic focusing/defocusing effects ($\delta \ln A_{V\mathrm{foc}}$) and 3-D anelastic effects ($\delta \ln A_{Q\mathrm{att}} + \delta \ln A_{Q\mathrm{foc}}$) on Love and Rayleigh wave amplitudes at 50, 100 and 200 s. In short-period surface waves (∼50 s), elastic focusing/defocusing effects are comparable to anelastic effects, that is, $\delta \ln A_{V\mathrm{foc}}$ is comparable to ($\delta \ln A_{Q\mathrm{att}} + \delta \ln A_{Q\mathrm{foc}}$). Elastic effects can cause an amplitude perturbation of approximately ±100 per cent while anelastic effects can result in an amplitude perturbation up to ±75 per cent in 50 s Rayleigh waves, and approximately ±50 per cent in 50 s Love waves. The anelastic effects in Rayleigh waves are relatively stronger than in Love waves at 50 s due to their stronger sensitivity in the low Q zone. Elastic and anelastic effects at this period in general show a negative correlation, consistent with SEM

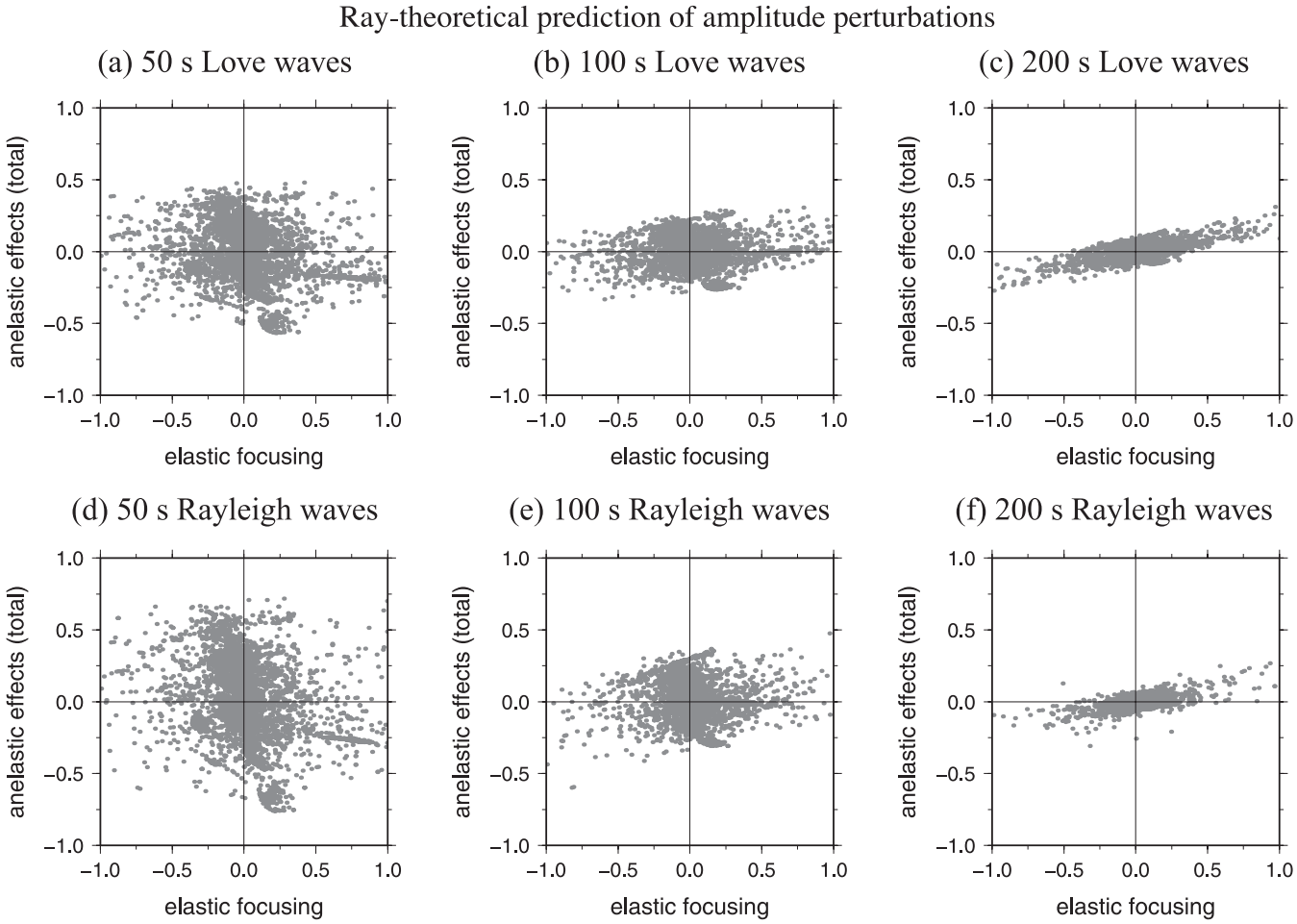

Figure 11. Ray theoretical predictions of 3-D anelastic and 3-D elastic effects on Love- and Rayleigh-wave amplitude variations at periods of 50, 100 and 200 s. At 50 s, (a) and (d), anelastic effects on amplitudes are comparable to elastic effects (focusing/defocusing), and they are, in general, negatively correlated. Anelastic effects on Rayleigh waves are stronger than Love waves due to their better sensitivity to the low Q zone in reference model. At 100 s, (b) and (e), anelastic effects become weaker and the correlation between anelastic and elastic effects becomes positive. At 200 s, (c) and (f), anelastic effects become very weak, and they are positively correlated with elastic effects.

simulations in 3-D models. In long-period surface waves (>100 s), elastic focusing/defocusing effects on amplitudes are the dominant effects, that is, $\delta \ln A_{V\mathrm{foc}} \gg (\delta \ln A_{Q\mathrm{att}} + \delta \ln A_{Q\mathrm{foc}})$. While elastic focusing can cause ±100 per cent amplitude perturbations in both Love and Rayleigh waves, anelastic effects cause approximately ±50 per cent amplitude perturbations in 100 s Rayleigh waves and ±35 per cent in 100 s Love waves, and anelastic perturbations decrease to less than ±25 per cent in both Love waves and Rayleigh waves at 200 s. At long periods, anelastic effects and elastic effects are positively correlated.

To better understand the relative importance of anelastic focusing/defocusing and anelastic attenuation in amplitude perturbations as a function of period, we plot anelastic attenuation, $\delta \ln A_{Q\mathrm{att}}$ and anelastic focusing, $\delta \ln A_{Q\mathrm{foc}}$, against elastic focusing, $\delta \ln A_{V\mathrm{foc}}$ in Fig. 12. In 50 s Rayleigh waves, as shown in Fig. 12(a), the effects of elastic focusing/defocusing and attenuation are comparable ($\delta \ln A_{V\mathrm{foc}} \sim \delta \ln A_{Q\mathrm{att}}$). In general, they are negatively correlated as expected. The correlation plot shows strong scattering. This is because attenuation ($\delta \ln A_{Q\mathrm{att}}$) depends upon perturbations in Q^{-1} while elastic focusing/defocusing depends upon the roughness of phase velocity perturbations ($\partial_y^2 \delta \ln c$). Although $\delta \ln Q^{-1}$ and $\delta \ln c$ are correlated, $\delta \ln Q^{-1}$ (Fig. 9b) and the roughness of $\delta \ln c$ (Fig. 10a) are not well correlated. In Fig. 12(b), we compare anelastic focusing/defocusing effects with elastic focusing/defocusing effects, and show that they are well correlated as expected based upon the correlation between the roughness maps (Fig. 10). Note

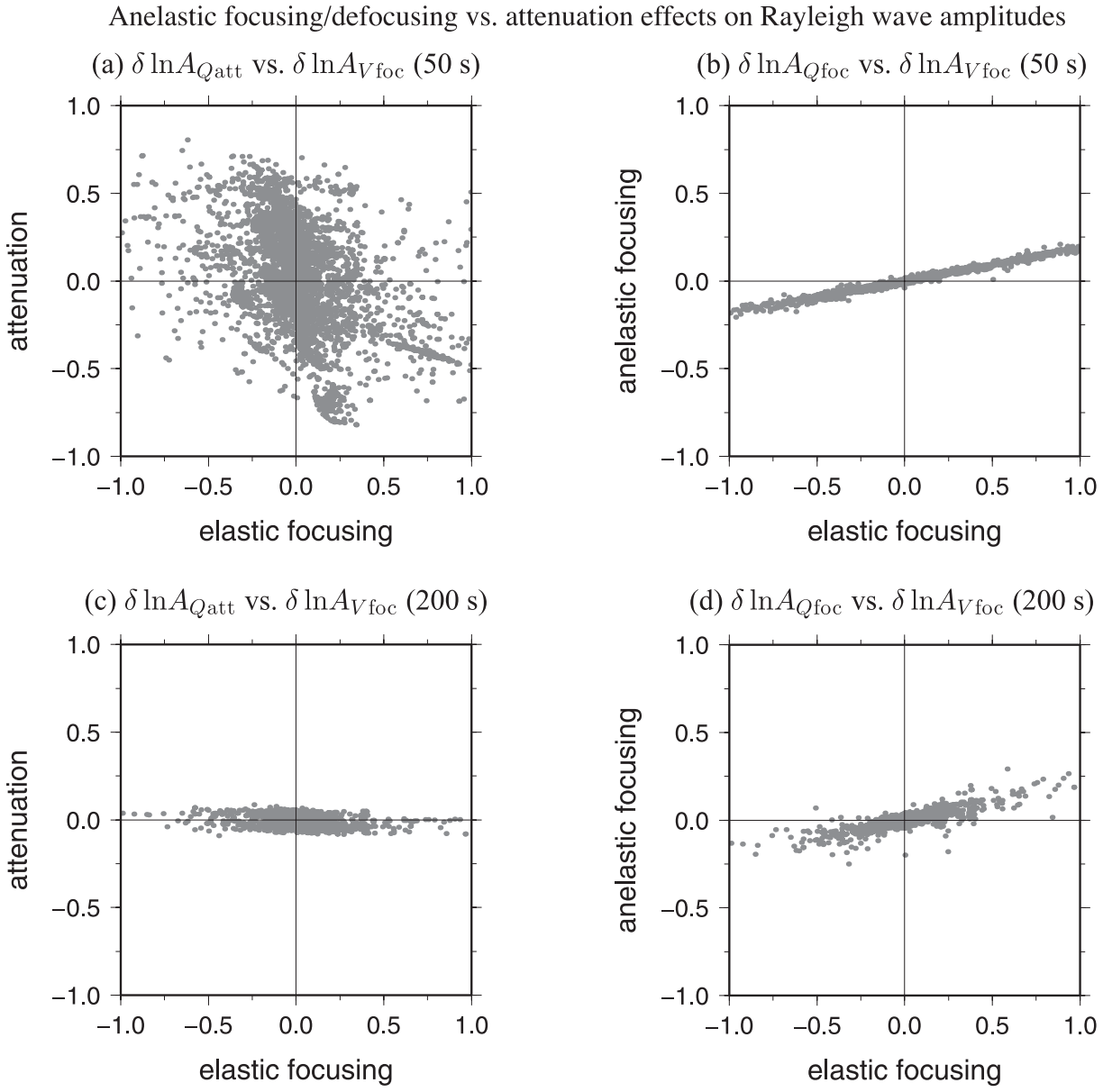

Figure 12. Comparison of anelastic attenuation ($\delta \ln A_{Q\mathrm{att}}$) and anelastic focusing/defocusing effects ($\delta \ln A_{Q\mathrm{foc}}$) on Rayleigh wave amplitudes. (a) Anelastic attenuation ($\delta \ln A_{Q\mathrm{att}}$) versus elastic focusing/defocusing ($\delta \ln A_{V\mathrm{foc}}$) on 50 s Rayleigh wave; they are comparable and, in general, negatively correlated. (b) Anelastic focusing/defocusing ($\delta \ln A_{Q\mathrm{foc}}$) versus elastic focusing/defocusing ($\delta \ln A_{V\mathrm{foc}}$), $\delta \ln A_{Q\mathrm{foc}}$ is much weaker than $\delta \ln A_{V\mathrm{foc}}$ and they are positively correlated. (c) and (d) are the same as (a) and (b) but for 200 s Rayleigh waves. At long periods, anelastic attenuation is the least significant effect, that is, $\delta \ln A_{Q\mathrm{att}} < \delta \ln A_{Q\mathrm{foc}} < \delta \ln A_{V\mathrm{foc}}$.

the roughness $\partial_y^2 \delta \ln c$ and $\partial_y^2 \delta \ln Q^{-1}$ have opposite signs and the $\ln(\omega/\omega_0)$ term in eq. (8) is negative as we consider wave frequency lower than reference frequency of 1 Hz. Therefore the correlation between elastic focusing and anelastic focusing effects is positive.

Ray theoretical calculations show anelastic attenuation and anelastic focusing/defocusing effects have different frequency dependence. Anelastic attenuation decreases quickly with increasing wave period. At 50 s, anelastic attenuation in Rayleigh waves is comparable to elastic focusing/defocusing, while at 200 s, anelastic attenuation is almost negligible compared with elastic focusing/defocusing ($\delta \ln A_{V\mathrm{foc}} \gg \delta \ln A_{Q\mathrm{att}}$) as shown in Figs 12(a) and (c). The decrease of anelastic attenuation with wave period is expected as long-period waves experience fewer cycles compared to short-period waves. However, anelastic focusing/defocusing is much less frequency-dependent than anelastic attenuation. In Fig. 12(d), anelastic focusing/defocusing effects ($\delta \ln A_{Q\mathrm{foc}}$) is about 20 per cent of the elastic focusing/defocusing effects ($\delta \ln A_{V\mathrm{foc}}$) in 200 s Rayleigh waves, this ratio is close to the ratio at 50 s. The frequency-independent ratio between elastic and anelastic focusing is a result of largely frequency-independent correlation between velocity and Q models. The correlation coefficient between the roughness field of phase velocity and roughness field of Q^{-1} is -0.99 for 50 s Rayleigh waves and -0.92 for 200 s Rayleigh waves.

We have assumed that mantle heterogeneities in wave speed and anelasticity are caused by temperature perturbations; therefore, the wave speed and anelasticity models as well as their roughness maps are well correlated. In the mantle, variations in composition, water content and partial melting may also introduce seismic heterogeneities with roughness structures that may be different from those caused by purely thermal (diffusion) process. In Fig. 13, we vary the roughness of the wave speed and Q models and compare elastic and anelastic ray theoretical amplitudes. The smoother degree-12 models used in the calculations are the same as the degree-20 models shown in Fig. 9 but with structures limited to spherical harmonic degrees $l \leq 12$. Compared to calculations in degree-20 models (Fig. 11), the scatterplots in Fig. 13 show that elastic (or anelastic) focusing effects become weaker in a smoother model where spherical harmonic degree $l > 12$ structures are excluded. This is expected because overall model perturbations are weaker in degree-12 models. The correlation between elastic and anelastic effects also becomes weaker when we compare calculations in degree-12 wave speed model and degree-20 Q model (or in degree-20 wave speed model and degree-12 Q model). However, the relative significance of elastic and anelastic effects as well as their frequency-dependent correlation are not particularly sensitive to model roughness: at 50 s, the correlation is largely negative and it becomes positive at longer periods.

In conclusion, ray theoretical calculations confirm that elastic focusing/defocusing effects on surface wave amplitudes caused by 3-D wave speed structures are comparable to anelastic effects caused by 3-D Q structures at short periods (∼50 s); at longer periods

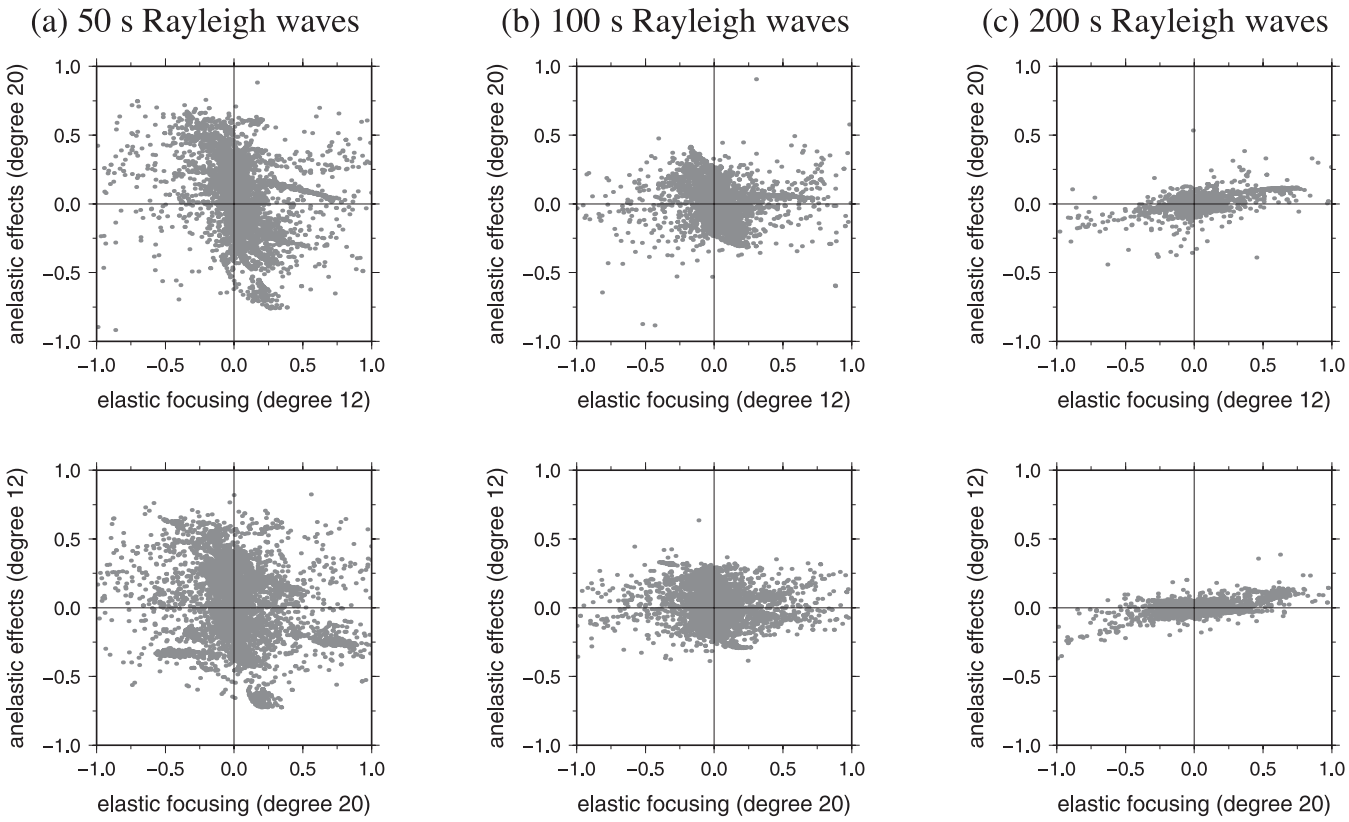

Figure 13. Comparison of elastic and anelastic effects calculated in models with different model roughness. The degree-20 models are the same as in Fig. 9, and degree-12 models are the same as degree-20 models but with structures limited to spherical harmonic degree $l \leq 12$. Top row in each column shows elastic focusing in degree-20 model versus anelastic effects (attenuation and anelastic focusing) in degree-12 model. Bottom row shows elastic focusing in degree-12 model versus anelastic effects in degree-20 model. Compared to calculations in degree-20 models (Fig. 11), elastic (or anelastic) focusing effects become weaker in degree-12 models, and the correlation between elastic and anelastic effects also becomes weaker when we compare calculations in degree-12 wave speed model and degree-20 Q model (or in degree-20 wave speed model and degree-12 Q model). However, the relative significance of elastic and anelastic effects as well as their frequency-dependent correlation are not particular sensitive to model roughness.

(>100 s), elastic focusing/defocusing effects become dominant. Attenuation effects decrease quickly with wave period and become the least significant effects on amplitude perturbations at long periods, weaker than anelastic focusing/defocusing effects. Our calculations suggest that both elastic focusing and anelastic focusing effects need to be taken into account when long-period surface wave amplitude data are used in tomographic studies. The effects can be accounted for by joint inversions of wave speed and Q structure using finite-frequency sensitivity kernels in anelastic media (Zhou 2009).

6 EFFECTS OF MINERALOGICAL PARAMETERS

The construction of the 1-D reference Q model and the 3-D Q model both depend upon mineralogical parameters. In this section, we experiment with two additional parameter sets to examine the dependence of 3-D anelastic effects on mineralogical parameters. The additional sets of mineralogical parameters, M_L and M_H, are shown in Table 3, and their corresponding 1-D Q models, $Q1DM_L$ and $Q1DM_H$, are plotted in Fig. 14. Compared with PREM Q profile, $Q1DM_L$ has much smaller Q values while $Q1DM_H$ has overall larger Q values. The PREM-like 1-D Q model $Q1DM_M$ is the model we used in Sections 3 and 4. Following the same algorithm discussed in Section 2, we use the additional parameter sets (M_L and M_H) to construct the corresponding 3-D Q models, $Q3DM_L$ and $Q3DM_H$, from the same 3-D wave speed model S20RTS. The 3-D Q models at a depth of 100 km are shown in Fig. 15. We simulate wave propagation in these two additional global Q models and make amplitude measurements following the same process as described in Section 3.

Table 3. Mineralogical parameters used in different anelasticity (Q) models.

Parameter set	E^* (KJ mol^{-1})	V^* (cm^3 mol^{-1})	A
M_L	420	19	1.394
M_M	470	17	1.394
M_H	520	15	1.394

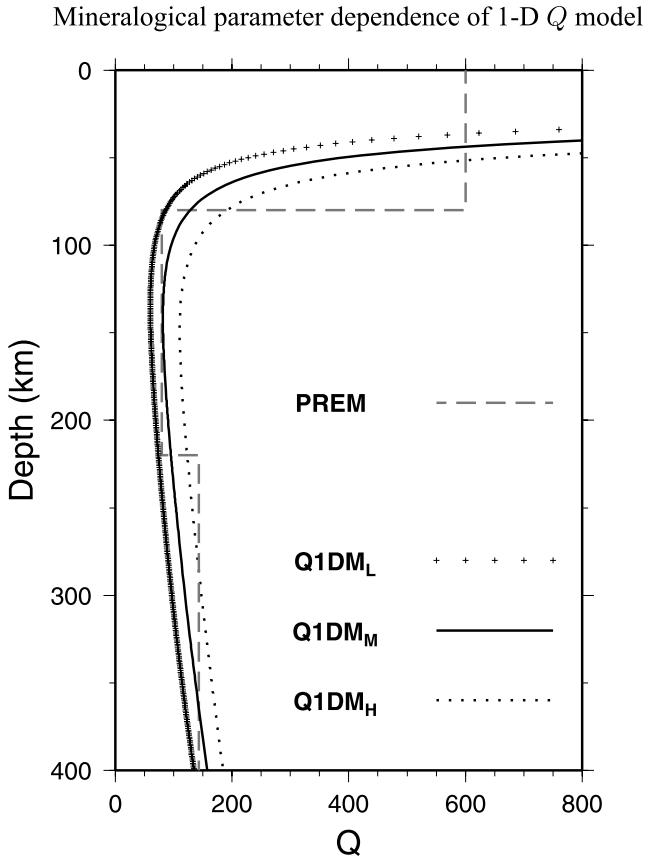

Figure 14. Reference Q models constructed using three different mineralogical parameter sets (Table. 3). Q values in $Q1DM_M$ are moderate and comparable to PREM at depths between 80 and 220 km, Q values are higher than PREM in model $Q1DM_H$ and lower than PREM in model $Q1DM_L$. PREM Q model is plotted in grey dashed line for reference.

Comparisons of 3-D elastic effects and 3-D anelastic effects on both Love waves and Rayleigh waves are shown in Fig. 15 as a function of period (50, 100, 150 and 200 s) for each mineralogical parameter set. The elastic focusing/defocusing effects on amplitudes (black bars) are identical in these three groups but the anelastic effects (grey bars) are associated with 3-D Q models generated using different mineralogical parameter sets. The values above each bar are average absolute amplitude perturbations ($|\delta \ln A|$).

Our measurements show that 3-D anelastic effects on short-period surface waves depend upon mineralogical parameters. For 50 s Love waves in model $Q3DM_L$ (parameter set M_L), the average amplitude perturbation $|\delta \ln A|$ caused by 3-D Q structures is 0.14, this value decreases to 0.12 in model $Q3DM_M$ and to 0.11 in model $Q3DM_H$. A similar pattern is shown in 50 s Rayleigh waves: the average amplitude perturbation $|\delta \ln A|$ caused by 3-D Q structures is 0.22 in model $Q3DM_L$, stronger than amplitude perturbations caused by 3-D wave speed structures (0.20) and decrease to 0.19 in $Q3DM_M$ and 0.15 in model $Q3DM_H$. At short periods, the dominant effect of 3-D Q structures is anelastic attenuation which depends upon δQ^{-1}. While fractional perturbations $\delta \ln Q^{-1}$ are the weakest in $Q3DM_L$, absolute perturbations δQ^{-1} are the largest among the models. The effects of variations in mineralogical parameters on anelastic amplitude perturbations are in general small, especially at longer periods (>100 s). This is because anelastic focusing becomes the dominant anelastic effect at long periods, and it depends upon the roughness of perturbations in Q^{-1} which do not vary greatly with mineralogical parameters and, moreover, anelastic attenuation and anelastic focusing/defocusing have opposite effects on amplitudes.

7 EFFECTS OF MEASUREMENT TECHNIQUES

We have used Slepian multitapers to measure amplitude variations in frequency domain. The Slepian multitaper method (MTM) has been introduced in surface wave measurements to reduce bias in spectral estimates (e.g. Laske & Masters 1996; Zhou *et al.* 2004). In Fig. 16, we compare amplitude measurements of 50, 100 and 200 s Rayleigh waves made with box-car tapers, cosine (Hann) tapers and Slepian multitapers. The comparisons show that amplitude measurements are dependent upon measurement techniques. This is because different tapers emphasizes different part of the seismogram in the measurement window. The differences in measurements can be minimized when when surface waves group energy at measurement frequency arrives approximately at the centre of the time window. In practice, the length of the time window is

determined by spectra resolution, and arrival-centred measurement windows often include higher-mode energy.

In conclusion, surface wave amplitude measurements are sensitive to measurement techniques. In traditional ray theory, the effects of measurement techniques can not be accounted for. Finite-frequency kernels that account for the effects of measurement technique and detailed comparison between SEM measurements and finite-frequency kernel predictions as well as ray theoretical predictions will be discussed in a separate paper.

8 DISCUSSION AND CONCLUSION

We investigate the effects of lateral variations in both wave speed and anelastic structure (Q) on surface wave amplitudes. Assuming that mantle heterogeneities are dominantly thermal and current tomographic models are accurate in order of magnitude, we construct 3-D earth models and compute synthetic seismograms using a spectral element method (Komatitsch & Tromp 1999, 2002a,b). We compare surface wave amplitude perturbations caused by 3-D wave speed structure with those caused by 3-D anelastic structure. The comparison shows that 3-D anelastic effects on amplitudes are significant only in short-period (∼50 s) surface waves, and become less significant in long-period (>100 s) surface waves. The elastic and anelastic effects on amplitude are negatively correlated at short period and the correlation becomes positive at long period because anelastic focusing/defocusing associated with anelastic dispersion becomes stronger than anelastic attenuation.

We calculate ray theoretical amplitude perturbations of surface waves due to elastic focusing/defocusing ($\delta \ln A_{V\mathrm{foc}}$), attenuation ($\delta \ln A_{Q\mathrm{att}}$) and anelastic focusing/defocusing ($\delta \ln A_{Q\mathrm{foc}}$). The calculations confirm that (1) at short period (∼50 s), anelastic attenuation is comparable with elastic focusing/defocusing ($\delta \ln A_{Q\mathrm{att}} \sim \delta \ln A_{V\mathrm{foc}}$) on surface wave amplitudes, but decrease rapidly with increasing wave period; (2) at longer period (>100 s), anelastic attenuation is less significant than anelastic focusing/defocusing ($\delta \ln A_{Q\mathrm{att}} < \delta \ln A_{Q\mathrm{foc}}$) and (3) anelastic focusing is positively correlated with elastic focusing if mantle heterogeneities are dominantly thermal. The frequency dependence of anelastic amplitude perturbations is, in general, not sensitive to mineralogical parameters used in thermal models, especially at long periods (>100 s).

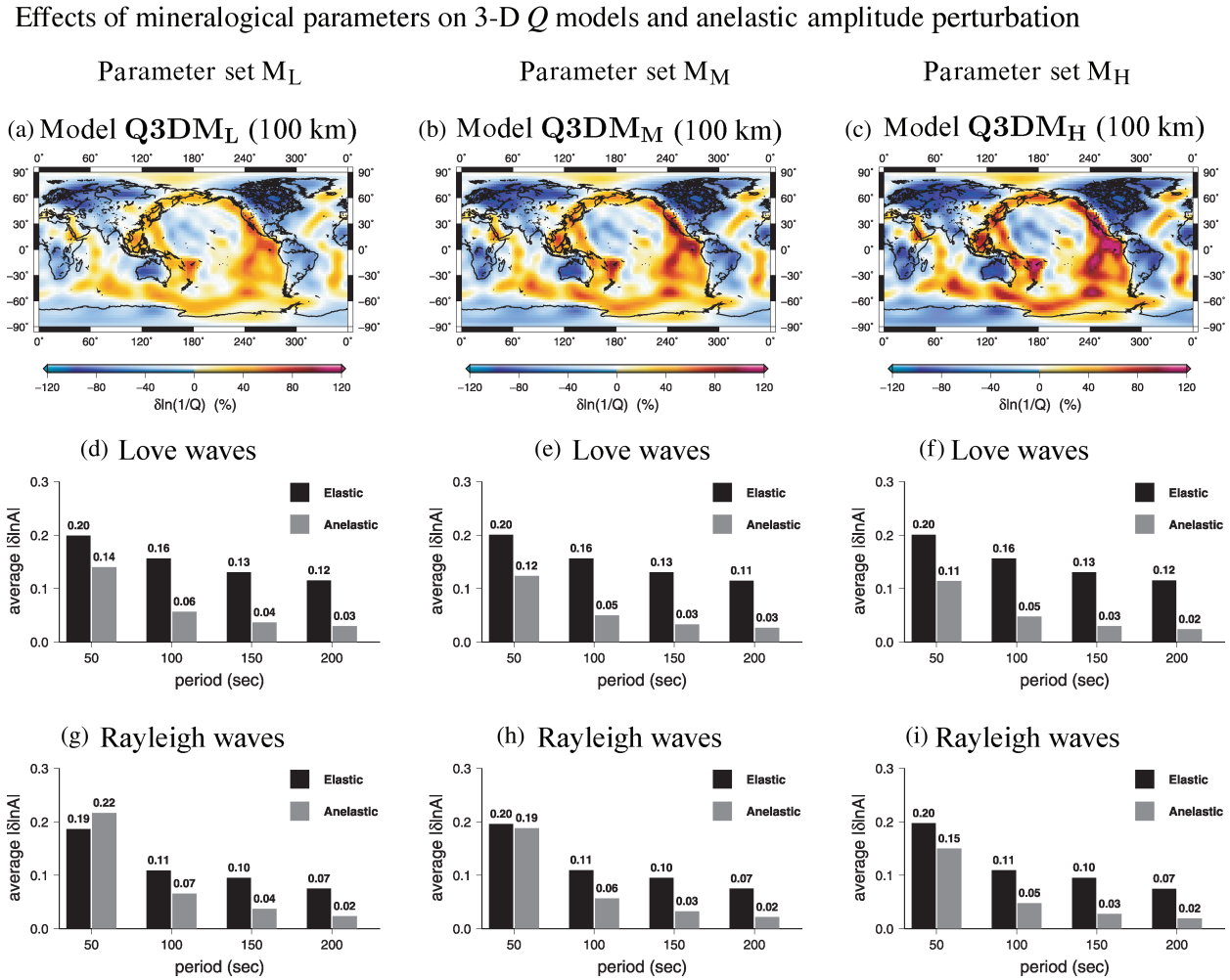

Figure 15. Anelastic effects on surface wave amplitudes measured in three 3-D Q models generated using mineralogical parameter sets $\mathrm{M_L}$, $\mathrm{M_M}$, and M_H. (a), (b) and (c) are maps of perturbations in Q^{-1} ($\delta \ln Q^{-1}$) at a depth of 100 km, the corresponding 1-D reference Q models are shown in Fig. 14. (d), (e) and (f) are comparisons between anelastic effects (grey bars) and elastic effects (black bars) on amplitude perturbations of Love waves. Amplitude perturbations shown above each bar are the average absolute values, $|\delta \ln A|$. (g), (h) and (i) are the same as (d), (e) and (f) but for Rayleigh waves. Measurements with large error bars have been excluded. Although fractional perturbations in Q^{-1} are the smallest in model $\mathrm{Q3DM_L}$, the absolute amplitude perturbations are the largest among the models due to the associated low Q values in the reference model $\mathrm{Q1DM_L}$ (Fig. 14).

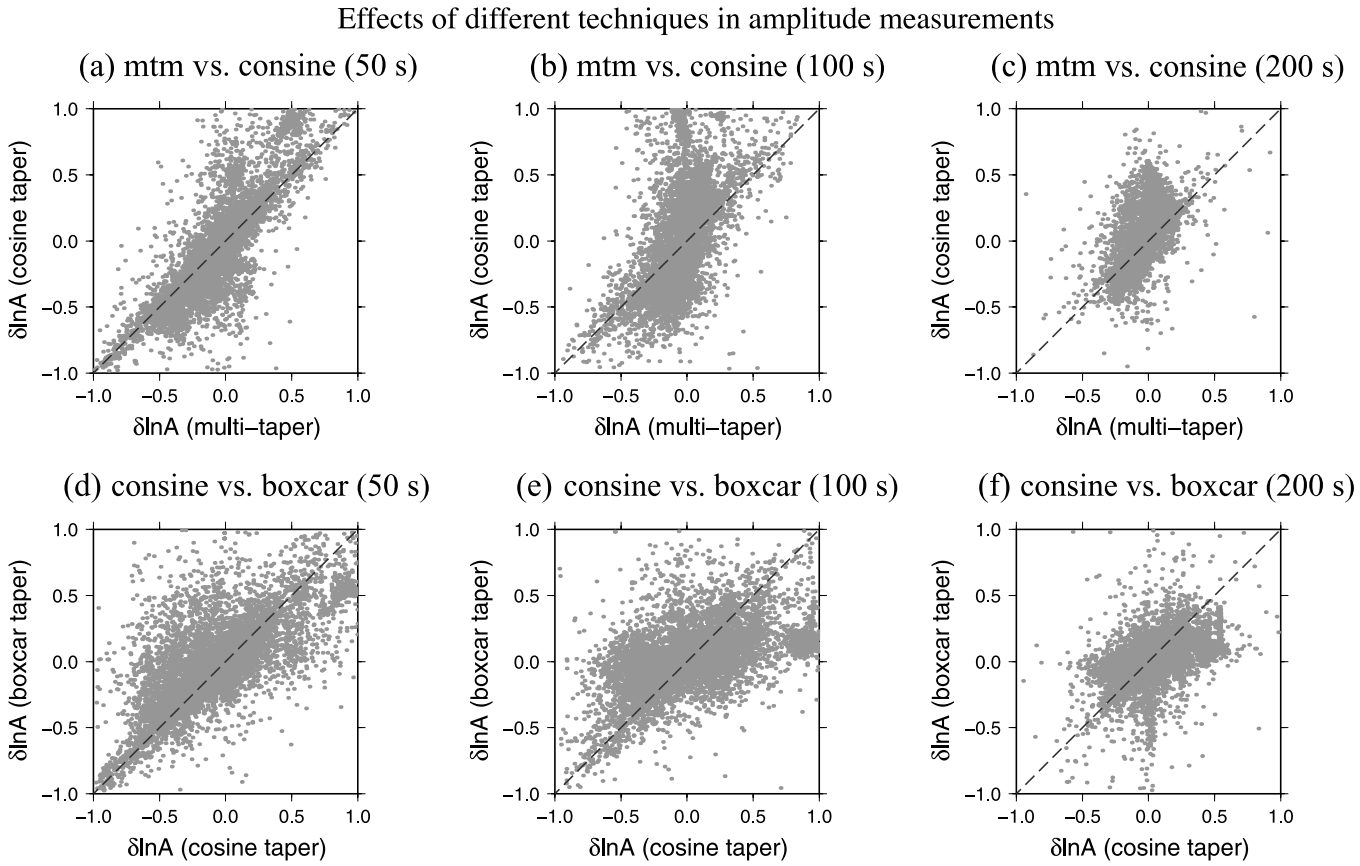

Figure 16. Comparison of Rayleigh-wave amplitude variations measured using different measurement techniques at periods of 50, 100 and 200 s. Panels (a), (b) and (c) are multitaper measurements (mtm) plotted against measurements made with cosine tapers. Panels (d), (e) and (f) are cosine taper measurements versus box-car taper measurements. Note that amplitude perturbations are dependent upon the measurement techniques.

ACKNOWLEDGMENTS

We wish to thank the two reviewers, Colleen Dalton and Daniel Peter, for their constructive comments, which greatly improved the manuscript. This research was financially supported by the US National Science Foundation under Grant EAR-1013617. All figures were generated using the Generic Mapping Tools (GMT) (Wessel & Smith 1995).

REFERENCES

Bhattacharyya, J., Masters G. & Shearer P., 1996. Global lateral variations of shear wave attenuation in the upper mantle, *J. geophys. Res.,* **101,** 22 273–22 289.

Dahlen, F.A. & Tromp, J., 1998. *Theoretical Global Seismology,* Princeton University Press, Princeton, NJ.

Dahlen, F.A. & Zhou, Y., 2006. Surface-wave group-delay and attenuation kernels, *Geophys. J. Int.,* **165,** 545–554.

Dalton, C. & Ekström, G., 2006a. Constraints on global maps of phase velocity from surface-wave amplitudes, *Geophys. J. Int.,* **167,** 820–826.

Dalton, C. & Ekström, G., 2006b. Global models of surface wave attenuation, *J. geophys. Res.,* **111,** B05317, doi:10.1029/2005JB003997.

Dalton, C., Ekström, G. & Dziewoński, A.M., 2008. The global attenuation structure of the upper mantle, *J. geophys. Res.,* **113,** B09303, doi:10.1029/2007JB005429.

Durek, J.J., Ritzwoller, M.H. & Woodhouse, J.H., 1993. Constraining upper mantle anelasticity using surface-wave amplitudes, *Geophys. J. Int.,* **114,** 249–272.

Dziewonski, A.M. & Anderson, D.L., 1981. Preliminary reference earth model, *Phys. Earth planet. Inter.,* **25,** 297–356.

Faul, U.H. & Jackson, I., 2005. The seismological signature of temperature and grain size variations in the upper mantle, *Earth planet. Sci. Lett.,* **234,** 119–134.

Gung, Y. & Romanowicz, B., 2004. Q tomography of the upper mantle using three-component long-period waveforms, *Geophys. J. Int.,* **157,** 813–830.

Isaak, D.G., 1992. High-temperature elasticity of iron-bearing olivines, *J. geophys. Res.,* **97,** 1871–1885.

Jackson, I., 2000. Laboratory measurements of seismic wave dispersion and attenuation: recent progress, in *Earth's Deep Interior: Mineral Physics and Tomography from the Atomic to the Global Scale,* Geophys. Monogr. Ser., Vol. 117, pp. 265–289, eds Karato S. *et al.* American Geophysical Union, Washington, DC.

Jackson, D.D. & Anderson, D.L, 1970. Physical mechanisms of seismic-wave attenuation, *Rev. Geophys.,* **8**(1), 1–63.

Jackson, I., Paterson, M.S. & Fitz Gerald, J.D., 1992. Seismic wave attenuation in Aheim dunite: an experiment study, *Geophys. J. Int.,* **108,** 517–534.

Jackson, I., Fitz Gerald, J.D., Faul, U.H. & Tan, B.H., 2002. Grain-size-sensitive seismic wave attenuation in polycrystalline olivine, *J. geophys. Res.,* **107**(B12), 2360, doi:10.1029/2001JB001225.

Kanamori, H. & Anderson, D.L., 1977. Importance of physical dispersion in surface-wave and free-oscillation problems—review, *Rev. Geophys. Space Phys.,* **15,** 105–112.

Karato, S.-I., 1993. Importance of anelastic in the interpretation of seismic tomography, *Geophys. Res. Lett.,* **20**(15), 1623–1626.

Karato, S.-I., 2003. Mapping water content in the upper mantle, in *Inside the Subduction Factory,* Geophys. Monogr. Ser., Vol. 138, pp. 135–152, ed. Eiler, J., American Geophysical Union, Washington, DC.

Karato, S. & Spetzler, H.A., 1990. Defect microdynamics in mineral and solid-state mechanisms of seismic wave attenuation and velocity dispersion in the mantle, *Rev. Geophys.,* **28,** 399–421.

Komatitsch, D. & Tromp, J., 1999. Introduction to the spectral-element method for 3-D seismic wave propagation, *Geophys. J. Int.,* **139,** 806–822.
Komatitsch, D. & Tromp, J., 2002a. Spectral-element simulations of global seismic wave propagation—I. Validation, *Geophys. J. Int.,* **149,** 390–412.
Komatitsch, D. & Tromp, J., 2002b. Spectral-element simulations of global seismic wave propagation—II. Three-dimensional models, oceans, rotation and self-gravitation, *Geophys. J. Int.,* **150,** 303–318.
Laske, G. & Master, G., 1996. Constraints on global phase velocity maps from long-period polarization data, *J. geophys. Res.,* **101**(B7), 16 059–16 075.
Liu, H.P., Anderson, D.L. & Kanamori, H., 1976. Velocity dispersion due to anelasticity: implications for seismology and mantle composition, *Geophys. J. R. astr. Soc.,* **47,** 41–58.
Master, G. & Richards-Dinger, K., 1998. On the efficient calculation of ordinary and generalized spherical harmonics, *Geophys. J. Int.,* **135,** 307–309.
Ritsema, J. & Van Heijst, H.J., 2000. Seismic imaging of structural heterogeneity in Earth's mantle: evidence for large-scale mantle flow, *Sci. Prog.,* **83,** 243–259.
Romanowicz, B., 1995. A global tomographic model of shear attenuation in the upper mantle, *J. geophys. Res.,* **100,** 12 375–12 394.
Romanowicz, B., 1998. Attenuation tomography of the Earth's mantle: a review of current status, *Pure appl. Geophys.,* **153,** 257–272.
Ruan, Y. & Zhou, Y., 2010. The effects of 3-D anelasticity (Q) structure on surface wave phase delays, *Geophys. J. Int.,* **181,** 479–492.
Savage, B., Komatitsch, D. & Tromp, J., 2010. Effects of 3D attenuation on seismic wave amplitude and phase measurements, *Bull. seism. Soc. Am.,* **100**(3), 1241–1251, doi:10.1785/0120090263.
Selby, N.D. & Woodhouse, J.H., 2000. Controls on Rayleigh wave amplitudes: attenuation and focusing, *Geophys. J. Int.,* **142,** 933–940.
Selby, N.D. & Woodhouse, J.H., 2002. The Q structure of the upper mantle: constraints from Rayleigh wave amplitudes, *J. geophys. Res.,* **107**(B5), 2097, doi:10.1029/2001JB000257.
Slepian, D., 1978. Prolate spheroidal wave functions, Fourier analysis and uncertainty—V: the discrete case, *Bell Syst. Tech. J.,* **57,** 1371–1429.
Wessel, P. & Smith, W.H.F., 1995. New Version of the Generic Mapping Tools Released, *EOS, Trans. Am. geophys. Un.,* **76,** 329.
Woodhouse, J.H. & Wong, Y.K., 1986. Amplitude, phase and path anomalies of mantle waves, *Geophys. J. R. astr. Soc.,* **87,** 753–773.
Yang, Y. & Forsyth, D.W., 2006. Regional tomographic inversion of amplitude and phase of Rayleigh waves with 2-D sensitivity kernels, *Geophys. J. Int.,* **166,** 1148–1160.
Zhou, Y., 2009. Surface-wave sensitivity to 3-D anelasticity, *Geophys. J. Int.,* **178,** 1403–1410.
Zhou, Y., Dahlen, F.A. & Nolet, G., 2004. Three-dimensional sensitivity kernels for surface wave observables, *Geophys. J. Int.,* **158,** 142–168.

APPENDIX A: CALCULATION OF AMPLITUDE FOCUSING

In the computation of the focusing/defocusing of surface wave amplitudes, we calculate the second spatial derivative (roughness) of perturbations in both phase velocity and Q models. In spherical coordinates, the surface Laplacian can be written as

$$\nabla^2\psi = \frac{\partial^2\psi}{\partial\theta^2} + \cot\theta\frac{\partial\psi}{\partial\theta} + \frac{1}{\sin^2\theta}\frac{\partial^2\psi}{\partial\phi^2}, \tag{A1}$$

where ψ represents the perturbation field of phase velocity or Q^{-1}. We expand the perturbation field using spherical harmonics

$$\psi(\theta,\phi) = \sum_{l=0}^{\infty}\left[a_{l0}X_{l0} + \sqrt{2}\sum_{m=1}^{l}X_{lm}(a_{lm}\cos m\phi + b_{lm}\sin m\phi)\right], \tag{A2}$$

where X_{lm} is the spherical harmonics (Dahlen & Tromp 1998, Appendix B). The roughness of the function, $\nabla^2\psi$, can then be expressed in terms of the real spherical harmonics X_{lm} and its derivative $\mathrm{d}X_{lm}/\mathrm{d}\theta$,

$$\frac{1}{\sin^2\theta}\frac{\partial^2\psi}{\partial\phi^2} = \sum_{l=0}^{\infty} -\frac{\sqrt{2}}{\sin^2\theta}\sum_{m=1}^{l}X_{lm}m^2(a_{lm}\cos m\phi + b_{lm}\sin m\phi), \tag{A3}$$

$$\cot\theta\frac{\partial\psi}{\partial\theta} = \sum_{l=0}^{\infty}\cot\theta\left[a_{l0}\frac{\mathrm{d}X_{l0}}{\mathrm{d}\theta} + \sqrt{2}\sum_{m=1}^{l}\frac{\mathrm{d}X_{lm}}{\mathrm{d}\theta}(a_{lm}\cos m\phi + b_{lm}\sin m\phi)\right], \tag{A4}$$

$$\begin{aligned}\frac{\partial^2\psi}{\partial\theta^2} = &\sum_{l=0}^{\infty}\left[a_{l0}\sqrt{l(l+1)}(\cot\theta X_{l1} + \sqrt{(l+2)(l-1)}X_{l2})\right]\\ &+\sum_{l=0}^{\infty}\left[\sqrt{2}\sum_{m=1}^{l}(-\frac{m}{\sin^2\theta}X_{lm} + m\cot\theta\frac{\mathrm{d}X_{lm}}{\mathrm{d}\theta}\right.\\ &\left.+\sqrt{(l+m+1)(l-m)}\frac{\mathrm{d}X_{l(m+1)}}{d\theta})\right.\\ &\left.\times(a_{lm}\cos m\phi + b_{lm}\sin m\phi)\right].\end{aligned} \tag{A5}$$

The roughness maps in Fig. 10 are calculated using eqs (A3)–(A5). In the calculation of the path integrals in eqs (6) and (8), we rotate the coordinates such that source and receiver are on the equator, and only the colatitudinal second partial derivatives $\partial^2/\partial\theta^2$ are needed after rotation.

The colatitudinal derivatives $\mathrm{d}X_{lm}/\mathrm{d}\theta$ are calculated using a pair of coupled recurrence relations (Master & Richards-Dinger 1998)

$$X_{l(m-1)} = -\frac{\mathrm{d}X_{lm}/\mathrm{d}\theta + m\cot\theta X_{lm}}{\sqrt{(l+m)(l-m+1)}}, \tag{A6}$$

$$\frac{\mathrm{d}X_{l(m-1)}}{\mathrm{d}\theta} = (m-1)\cot\theta X_{l(m-1)} + \sqrt{(l+m)(l-m+1)}X_{lm}. \tag{A7}$$

For this recurrence relations, the stable iteration direction is downward from $m = l$ to $m = 0$; the starting values in this case are

$$X_{ll} = (-1)^l\left(\frac{2l+1}{4\pi}\right)^{1/2}\frac{\sqrt{(2l)!}}{2^l l!}(\sin\theta)^l, \tag{A8}$$

$$\frac{\mathrm{d}X_{ll}}{\mathrm{d}\theta} = l\cot\theta X_{ll}. \tag{A9}$$